Chapter – 3

Synthesis, Characterization, DNA/BSA Binding and Cytotoxicity Studies of Cu(II) and V(IV) Complexes Derived from Mannich Bases of Lawsone

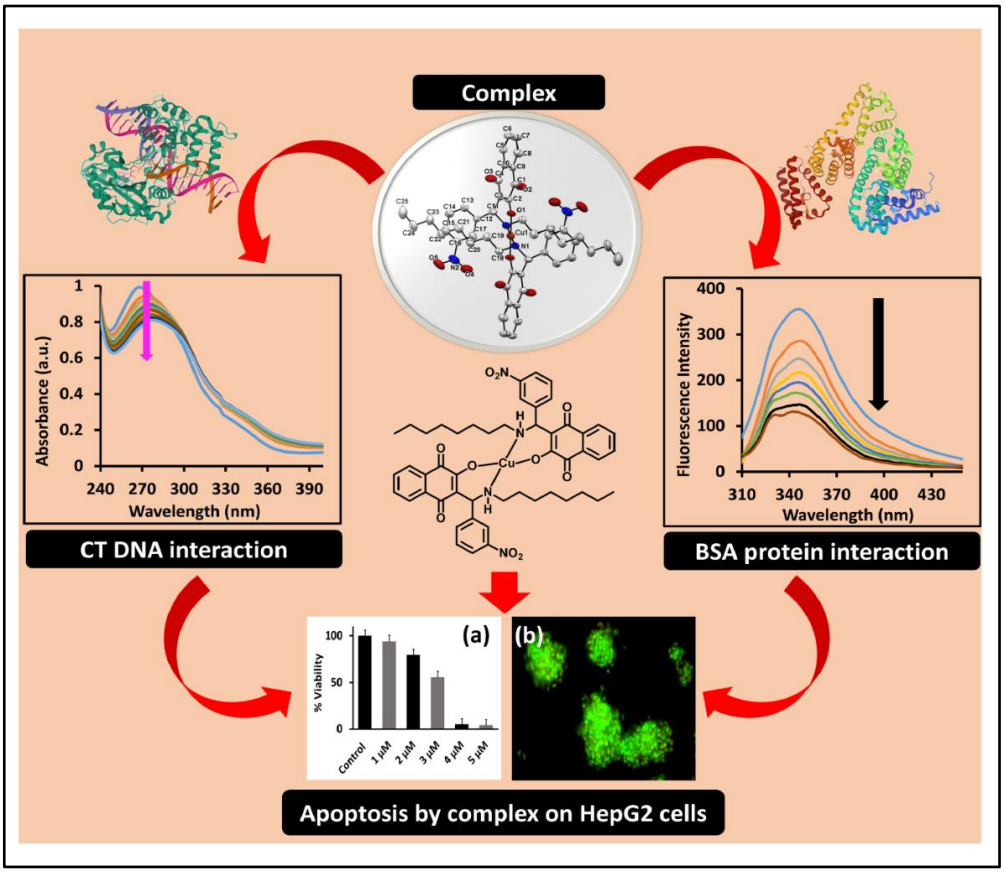

Published in *J. Mol. Struct.*, 2022, *1248*, 131508

3.1 Introduction

As stated in **chapters 1** and **2**, substances containing quinone exhibit a variety of pharmacological characteristics. Lawsone has the potential to attach to metal ions in various degrees of oxidation, coordinating metals in a bidentate manner and allowing them to be vital components of biological systems. The literature findings have shown that various metal complexes with lawsone showed higher biological activity than free lawsone. The biological activity of naphthoquinone may be increased by the addition of a nitrogen atom[1]. As discussed in **chapter 2**, the simplest approach to add a nitrogen atom to lawsone, sometimes referred to as a Mannich base, is by a Mannich reaction[2]. A new family of Mannich bases generated from lawsone with increased anticancer activity has just been disclosed [3]. Metal complexes derived from lawsone derivatives are known for their cytotoxic activities. Platinum (II) /Pt^{2+} complexes of 2-hydroxy (3-aminomethyl)-1,4-naphthoquinone, Ruthenium (II)-arene complexes of naphthoquinone and lawsone are known to have cytotoxic evolution against cancer cells[4–6]. Ferrocene modified lawsone mannich bases with anti-proliferative activity against cancer cells have also been reported [7].

Researchers were prompted to investigate the possibilities of transition metals in the pharmaceutical sector by the fact that they are present in our bodies as mettalo-enzymes. Copper is one of the essential trace elements in the human body and plays crucial roles in many biological processes, enzyme regulations, structural and functional enhancement of proteins. Copper complexes have been investigated on the premise that endogenous metals may be less toxic to healthy cells than to cancer cells. Copper complexes that are anti-cancer active can work in several ways, including by binding to DNA, inducing apoptosis through the production of reactive oxygen species (ROS), and inhibiting topoisomerase-I. Some of the copper complexes are employed as a model molecule for the biological oxygen carrier system[8–10]. Similarly, vanadium complexes are under research for their probable use as therapeutics due to their insulin like behaviour[11]. It was also reported that the vanadium complex causes a reduction of hyperlipidemia and hypertension to suppress tumor cell growth[12,13]. Copper complexes of aminonaphthoquinone have been reported for antibacterial activity but it is less explored for anticancer activity while vanadium complexes of aminonaphthoquinones are not reported and explored [14].

In this investigation, several Cu(II) complexes that are anticancer active as well as a vanadium complex of 3-aminomethyl-1,4-naphthoquinone generated from lawsone mannich bases were successfully synthesized. The structures of these synthesized complexes were established based on FTIR, ESI-MS, UV-vis, and elemental analyses. The redox properties of the complexes were studied by cyclic voltammetry (CV). To understand the chemical environment and binding pattern around the metal center, EPR analyses were performed on all of the complexes. The geometry optimization and Frontier Molecular Orbital (FMO) analysis of the complexes were analyzed through DFT calculations. To get an insight into the charge distribution over complexes MEP surfaces computational tool was also scrutinized. The interactions of complexes towards biomolecules (CT-DNA and BSA) were explored in depth with the aid of UV-vis and fluorescence techniques to reveal their biological potential. Additionally, complexes **3-6's** *in vitro* anticancer activity was successfully assessed against the HepG2 cell line utilizing the MTT assay in conjunction with the measurement of apoptosis (AO/EB staining).

3.2 Results and Discussions

3.2.1 Synthesis of ligands and Cu(II) complexes

The ligands were synthesized in good yield from the reaction of lawsone with various amine and aldehydes using ethanol as a solvent under stirring at 30^{o}C **(chapter 2, section 2.2.1, scheme 2.1).** The structures of the ligands were confirmed by various spectroscopic and analytical techniques[3] **(chapter 2, section 2.2.2)**. All synthesized ligands were stable in the solid state. However, they tend to undergo decomposition in solution after a long period of time as reported in the literature [2].

Cu(II) **complexes 1-5** were obtained in good yield (70% to 81%) by refluxing ligands and copper acetate monohydrate in methanol **(scheme 3.1a)**. Ligands are yellow to red while Cu(II) complexes are greenish to brown. Similarly, the oxovanadium complex was prepared by a typical synthetic procedure. The methanolic aqueous solution of vanadyl sulfate was reacted with **8** and imidazole under reflux for 3 hr to give a brown color **complex 6** as shown in **scheme 3.1b** [15]**.** All complexes were stable in air at room temperature. The results of the elemental analysis was in good agreement with the proposed structure.

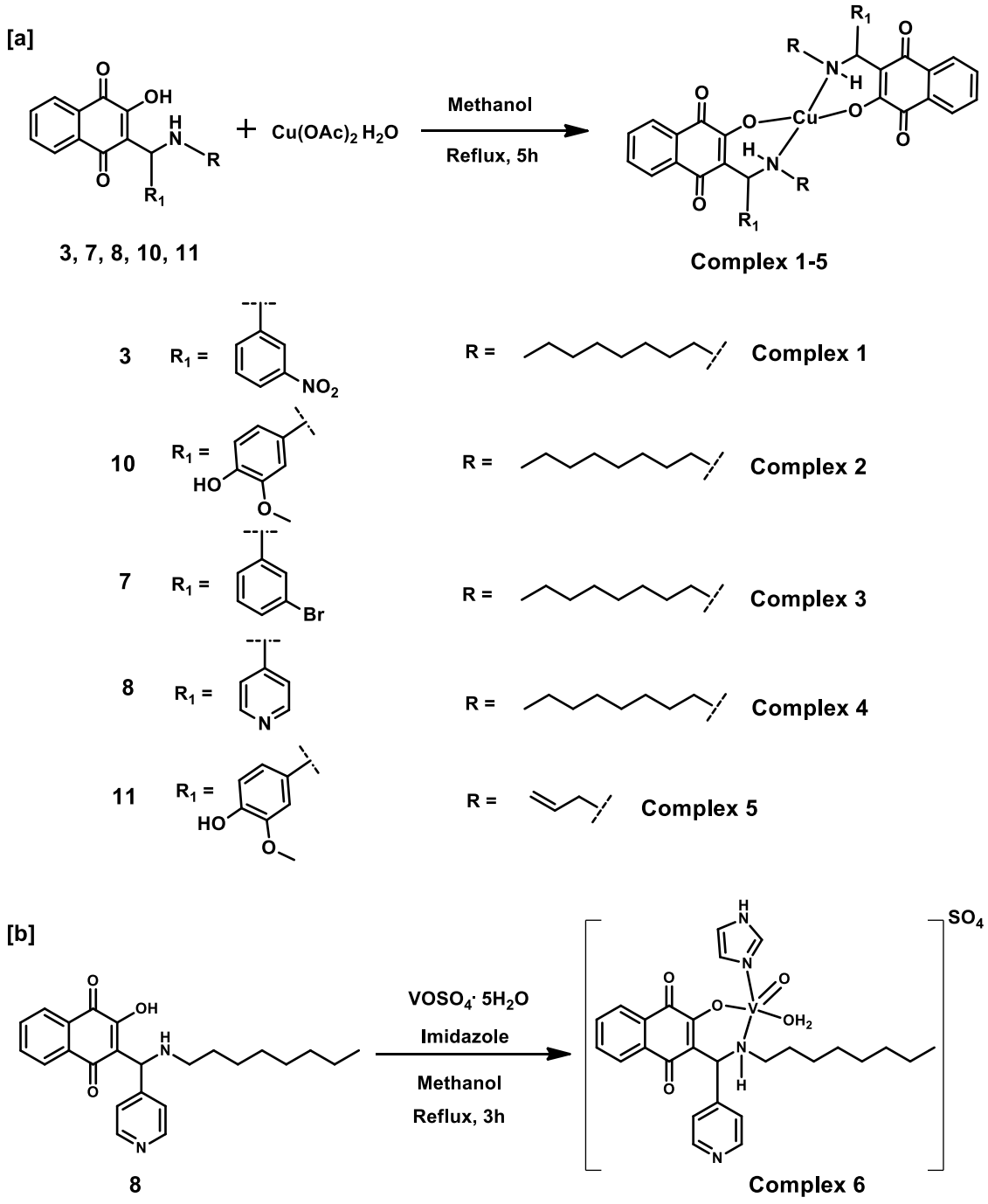

Scheme 3.1 Schematic for the synthesis of (a) complexes 1-5, and (b) complex 6

3.2.2 Crystal structure description

The molecular structure of **complex 1** was confirmed by single crystal X-ray diffraction analysis. The ORTEP view of **complex 1** with atom numbering is presented in **figure 3.1(a)** and crystal packing along a crystallographic axis is shown in **figure 3.1(b).** The selected bond angle and bond length are given in **table 3.1**. The crystallographic data and molecular structure refinement data are presented in **table 3.2**.

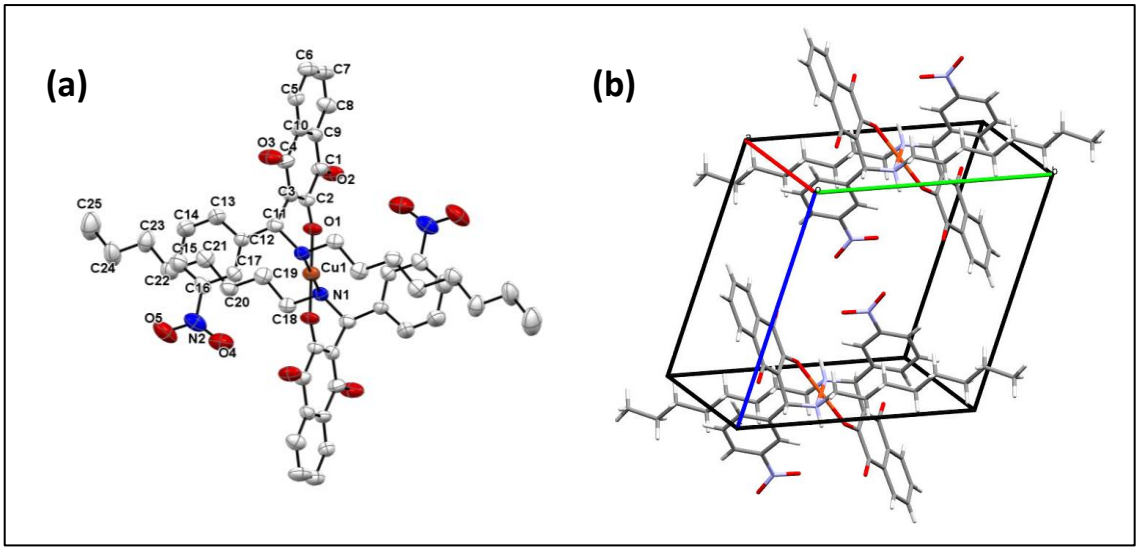

Figure 3.1: (a) ORTEP view of complex 1 with 50% probability (hydrogen atoms and solvent were omitted for clarity) and (b) crystal packing along *a* crystallographic axis of complex 1

Table 3.1 Selected bond length (Å) and bond angle (°) for complex 1.

Bond length (Å)	**XRD**	**DFT**
Cu1-O1	1.923(3)	1.9272
Cu1-O1^1	1.923(3)	1.9279
Cu1-N1	2.004(4)	2.0492
Cu1-N1^1	2.004(4)	2.0503
Bond angle (°)		
O1-Cu1-N1	87.94 (16)	87.619
O1^1-Cu1-N1^1	87.94 (16)	87.961
O1-Cu1-N1^1	92.06 (16)	92.1804
O1^1-Cu1-N1	92.06 (16)	92.2414
O1-Cu1-O1^1	180.0(2)	179.86
N1-Cu1-N1^1	180.0(2)	180.20

The central Cu(II) atom is in a trans N_2O_2 environment of two chelating ligands. Two deprotonated ligands **3** coordinates through the naphthalene-2-olate oxygen and secondary amine nitrogen atoms. It forms two six-membered chelate rings around the centrosymmetric copper atom. The complex crystallizes in the triclinic space group (P-1). The bond angles between O1-Cu1-N1 and O1-Cu1-N1^1 were found to be 87.94 (16)

and 92.06 (16) respectively, which indicated a slightly distorted square planar geometry of complex [16].

Table 3.2 Crystallographic data and structure refinement for complex 1

Empirical formula	$C_{52}H_{62}CuN_4O_{12}$
Formula weight	998.59
Temperature/K	293(2)
Crystal system	Triclinic
Space group	P-1
a/Å	10.0341(19)
b/Å	12.048(3)
c/Å	12.4074(19)
α/°	115.657(18)
β/°	111.087(15)
γ/°	90.500(16)
Volume/Å^3	1237.2(4)
Z	1
ρcalcg/cm^3	1.340
μ/mm^{-1}	0.508
F(000)	527.0
Crystal size/mm^3	0.3 × 0.2 × 0.2
Radiation	MoKα (λ = 0.71073)
2Θ range for data collection/°	6.688 to 57.658
Index ranges	$-13 \leq h \leq 6$, $-15 \leq k \leq 14$, $-14 \leq l \leq 16$
Reflections collected	5755
Independent reflections	4912 [R_{int} = 0.0507, R_{sigma} = 0.1430]
Data/restraints/parameters	4912/0/316
Goodness-of-fit on F^2	0.973
Final R indexes [I>=2σ (I)]	R_1 = 0.0810, wR_2 = 0.1653
Final R indexes [all data]	R_1 = 0.1543, wR_2 = 0.2280
Largest diff. peak/hole / e Å^{-3}	0.87/-0.66

The bond lengths between Cu-O (1.923(3) Å) and Cu-N (2.004(4) Å) were in the normal range compared to that Cu (II) complexes with a similar coordination environment [14,17]. The coordinating atoms lying on the same plane as the center atom with N1-Cu1-N1^1 and

O1-Cu1-O1[1] angles equal to 180° proves complex has square planar geometry. The bond angles and bond lengths obtained by the DFT study further proved the square planar geometry of complexes.

The intermolecular hydrogen bonding interaction is shown in **figure S3.1a.** The C6-H6----O4 hydrogen bonds are formed between hydrogen atoms of the naphthoquinone ring and oxygen of nitro group with a distance d (H---O) 2.660Å. The layered structure of **complex 1** along *b* crystallographic axis in a crystal lattice is shown in **figure S3.1b.**

3.2.3 Spectral characterization

The FT-IR spectra showed a broad band near 3450 to 3300 $cm^{-1}$for stretching frequencies of hydroxyl and secondary amine for ligands, while complexes showed a sharp band near 3450 to 3350 cm^{-1} **(figure 3.2)**. The new bands in the region of 3200 to 3300 cm^{-1}can be attributed to ν (N-H) [18,19]. These bands were not observed in free ligands.

The ~ 20 cm^{-1} shift in bending frequency of N-H around 1500 cm^{-1} was observed in complexes as compared to ligands. The carbonyl stretching (C=O) frequency was observed around 1670 cm^{-1}. It does not show shifting in stretching frequency as compared to ligand, which indicates it does not participate in complexation [20]. In the case of ligand **3** and **complex 1**, the symmetric and asymmetric stretching frequencies for the nitro group were observed at 1593 cm^{-1} and 1349 cm^{-1} respectively **(figure 3.2)**. In the far IR region, medium intensity bands at 500-530 cm^{-1} and 440-410 cm^{-1} were observed and it can be attributed to Cu-N and Cu-O vibrations respectively in all complexes. [21,22]. FT-IR overlay of **3** and **complex 1** is shown in **figure 3.2** while FT-IR spectra of other complexes are provided in the spectral data **(figure S3.2-S3.6)**.

In the FT-IR spectra of the **complex 6** absorption band at 3472 cm^{-1} assigned to N-H vibration involving coordination through the nitrogen of the secondary amine group, it also shows shifting in N-H bending frequency. The band at 1634 cm^{-1}can be assigned to υ(C=O) of the carbonyl group, while C=O stretch in the ligand **8** appears at 1679 cm^{-1} **(Figure S3.6).** This shift suggests that the oxygen atom of the carbonyl group may be involved in the binding of vanadium in the complex [23]. The V=O stretching frequency of **complex 6** was observed at 974 cm^{-1}, which is in the usual range previously reported

for the majority of oxovanadium(IV) complexes [15,24].

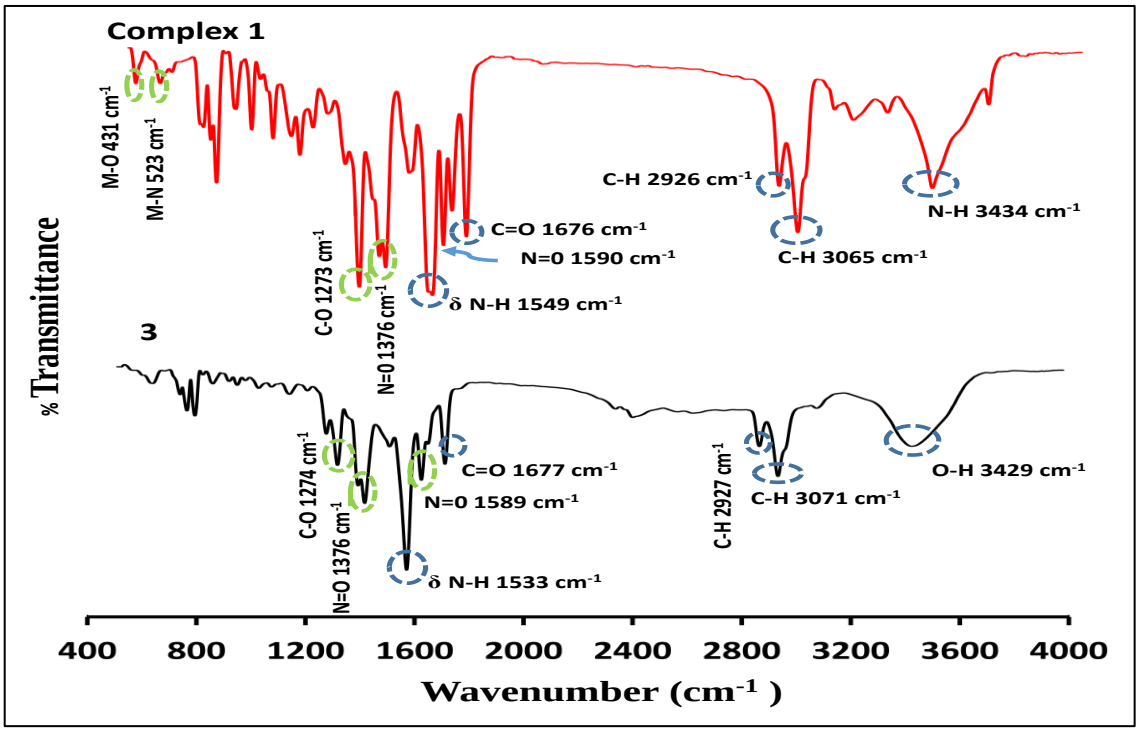

Figure 3.2 FT-IR spectra of complex 1, and ligand 3.

In addition, post-simulation analysis of the DFT calculated IR could provide a detailed view of the vibration associated with complexes. The calculated values are close to the experimentally observed data.

UV-Vis spectra of ligands and complexes were recorded in chloroform and are shown in **figure 3.3.** The electronic spectra of all ligands and complexes were recorded in chloroform ($CHCl_3$) while spectra of **complexes 5** and **6** were recorded in dimethyl sulfoxide (DMSO). The intense absorption band was observed between 450-490 nm for ligands**.** It can be attributed to n-π* transition of the lawsone quinoid ring oxygen atom [25]. These bands showed a blue shift and were observed between 425-435 nm for all **complexes 1-5**. An intense band at 436 nm was observed for **complex 6** which can be attributed to ligand-to-metal charge transfer (LMCT) of the naphthoquinone moiety to the metal ion [26,27]. The d-d transition band appears at 590 nm and 680 nm for **complexes 1-3** and **4-5** respectively **(inset figure 3.3a-3.3e).** It supports the square planar or distorted octahedral geometry for the Cu(II) complexes in solutions[28,29]. The low-intensity d-d absorbance band was observed at 856 nm for **complex 6.** It can be assigned to a $b_2(dxy) \rightarrow e_{\pi^*}$ (dxy; dyz) transitions VO^{2+} ion. These bands are typical for distorted

octahedral VO^{2+} complex [27,30]. The π-π* band was also observed for all ligands near 235-250 nm**,** which remains unaltered after complexation.

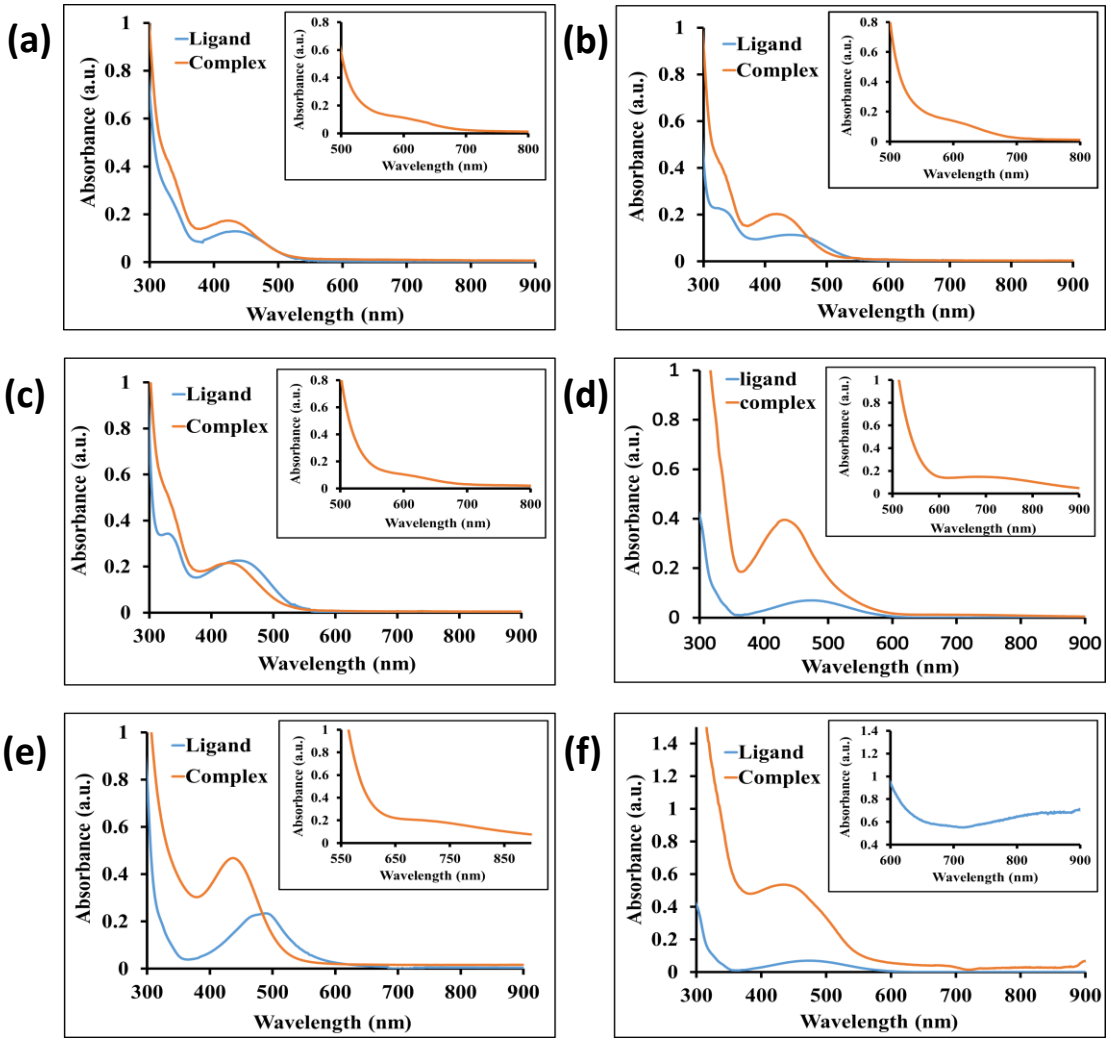

Figure 3.3 UV-Visible spectra of complexes (a) 1, (b) 2, (c) 3, (d) 4, (e) 5 and (f) 6 with corresponding ligands (6.6×10^{-5} M solution of ligands and complex, inset 1.0×10^{-3} M for Copper complex and 3.0×10^{-3} M for Vanadium complex).

The molar conductance of **complexes 1-6** recorded in DMSO (1.0×10^{-3} M) revealed their non-electrolytic nature. The molar conductance values are 6.67, 18.74, 6.26, 17.95 and 15.44 S cm^2 $mol^{-1}$for **complexes 1-5** respectively [21]. The molar conductance of **complex 6** was 114 S cm^2 mol^{-1} corresponding to 1:1 electrolyte [31].

The redox behavior of **complexes 4** and **6** were evaluated by cyclic voltammetry (CV) at room temperature in DMSO with tetrabutylammonium perchlorate as a supporting electrolyte. The CV of complexes depicted in **figure 3.4** was obtained versus ferrocene/ferrocenium. The data obtained for complexes **4 & 6** are depicted in **table 3.3**.

Table 3.3 Electrochemical data for complex 4 & 6 determined by CV in DMSO at a glassy carbon electrode; scan rate 0.1V/s and 0.3V/s for complex 4 & 6 respectively.

Compound	E_{p1c}(V)	E_{p2c}(V)	$E_{p1/2(3)}$(V)
Complex 4	-0.807	-1.343	-1.075
Complex 6	-0.773	-1.313	-0.725

The CV of **complexes 4** and **6** showed a quasi-reversible process attributed to the quinone group of the ligand. The CV of **complex 4** showed one characteristic wave for quinone of ligand (E_p around -1.4 V) confirming the interaction of naphthalene-2-olate oxygen in solution **(figure 3.4)** [2,26]. In CV of **complex 4** one irreversible peak was observed around -0.65 V, which can be assigned to Cu^{II}, $Cu^{II} \rightarrow Cu^{II}$, Cu^{I} process [26]. Similar behavior was also observed in presence of ferrocene/ferrocenium along with its characteristic redox potential peak $E_{p1/2}$ = 0.404 V of ferrocene [32].

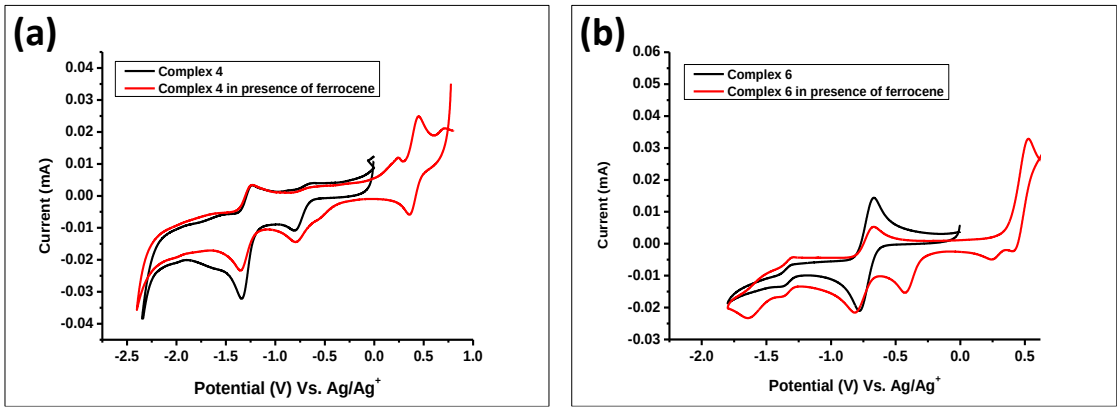

Figure 3.4 Cyclic voltammogram of (a) complex 4, and (b) complex 6 in DMSO in presence and absence of ferrocene as internal standard.

All the complexes have been characterized by ESI-MS in DMSO. The mass spectra of the complexes were in good agreement with the proposed structures. The mass spectrum of **complex 1** prominent peak at m/z 936.50 corresponds to molecular ion peak $[C_{50}H_{54}CuN_4O_{10}]^+$**(inset figure 3.5)**. Other fragment peaks for **complex 1** were observed at m/z 874.56, 438.05 which were assigned to $[C_{50}H_{54}N_4O_{10}]^+$ and $[C_{25}H_{27}N_2O_5]^{2+}$ moieties respectively **(figure 3.5)**.

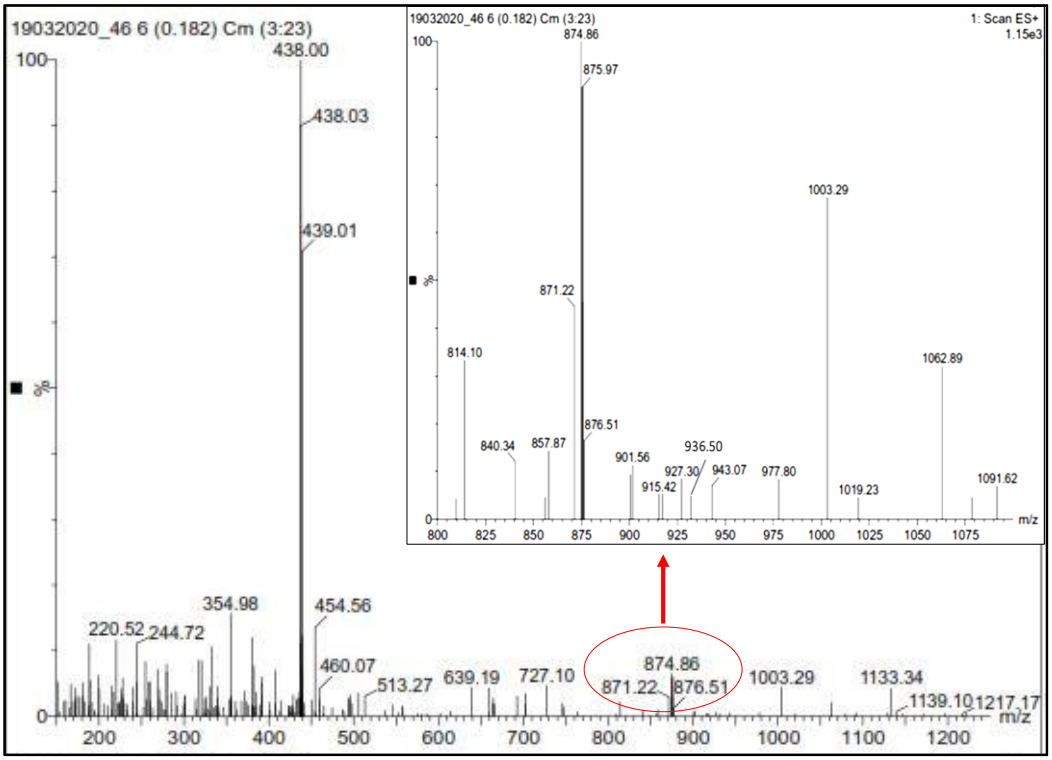

Figure 3.5 ESI-MS spectra of complex 1

The mass spectra of **complexes 2, 4,** and **5** exhibited a prominent peak at m/z 936, 848.19, and 790 corresponding to molecular ion peak $[C_{52}H_{60}CuN_2O_{10}]^+$, $[C_{48}H_{54}CuN_4O_6]^{2+}$ and $[C_{42}H_{36}CuN_2O_{10}]^{2-}$ respectively **(figure S3.7, S3.9, and S3.10)**. **Complex 3** showed a peak at m/z 1077 corresponding to $[C_{50}H_{54}Cl_2CuN_2O_6{\cdot}DMSO]^+$**(figure S3.8)**. It might have resulted from the replacement of weakly coordinated H_2O molecules by DMSO [33]. Similarly, mass spectra of **complex 6** exhibited a peak at m/z = 545 corresponding to molecular ion peak $[C_{27}H_{33}VN_4O_5]^+$ which confirms the formation of oxovanadium complex **(figure S3.11).**

To further investigate the coordination modes of Cu(II) and oxovanadium complexes EPR measurements were done at 77K in the solution state. The EPR spectra of **complexes 1** and **6** are shown in **figure 3.6a-3.64b.** and anisotropic g and A values obtained for **complexes 1-6** are given in **table 3.4**. The spectra of **complexes (1, 2, 3, and 5)** resolved four hyperfine lines of copper which indicate magnetic anisotropy in these systems and characteristics of monomeric Cu(II) complexes **(figure S3.12a, S3.12b, and S3.12d)** [34]. The EPR spectra of **complex 4** showed a single isotropic peak may be due to occupancy of an unpaired electron to degenerate p orbitals **(figure S3.12c)** [35].

The values of $g_{\parallel}$ and $g_{\perp}$ were in ranges 2.203-2.252 and 2.017-2.033 respectively. The complexes possess $g_{\parallel} < 2.3$ suggesting an appreciable metal-ligand covalent bonding [21,34]. The complexes demonstrated $g_{\parallel} > g_{\perp} > 2$ and $A_{\parallel} = (206.39\text{-}213.35) \times 10^{-4}\ cm^{-1}$, which revealed that unpaired electrons were mainly located in d_{x2-y2} orbital [14,21]. The empirical ratio of $g_{\parallel}$:$A_{\parallel}$ for all complexes is between 103-106 and g_0 = 2.06-2.10 suggested square planar geometry. The data was in good agreement with axially symmetrical Cu(II) complexes with square planar geometry [34,36,37].

Table 3.4 EPR parameters of complexes 1-6

Complex	$g_{\parallel}$	$g_{\perp}$	g_0	$A_{\parallel}$ ($\times 10^{-4}\ cm^{-1}$)	$A_{\perp}$ ($\times 10^{-4}\ cm^{-1}$)
1	2.2037	2.0172	2.0794	206.39	21.64
2	2.2069	2.0185	2.0638	213.04	19.61
3	2.2094	2.0179	2.0817	213.35	23.90
4	--	--	2.1035	--	--
5	2.2522	2.0337	2.1065	--	--
6	2.1056	2.0868	2.0930	165	34.4

In order to ascertain the oxidation state of vanadium, the X band EPR spectrum of complex **6** was recorded at liquid nitrogen temperature in DMSO **(figure 3.6b)**. The spectra exhibit an axially symmetrical hyperfine eight-line pattern that originates from d electron interaction with a nuclear spin I = 7/2. Thus spectra display well-resolved ^{51}V hyperfine lines and signal parameters for the complex are given in **table 3.4**. The $g_{\parallel} >> g_{\perp}$ and $A_{\parallel} >> A_{\perp}$ relationships are characteristics of an axially compressed d_{xy} configuration. Thus, an oxidation state of +4 can be assigned to vanadium similar to other oxovanadium complexes reported earlier [15,23].

The powder X-ray diffraction (XRD) pattern of Cu(II) **complex 4** and oxovanadium **complex 6** overlayed with ligand **8** are shown in **figure 3.6c** and **3.6d** respectively. The diffraction pattern was recorded from 2θ = 10-50°. The ligand **8** showed the peak at 2θ= 12.43°, 13.69°, 14.20°, 16.43°, 17.95°, 18.45°, 20.58°, 21.34°, 22.25°, 22.96°, 23.87°, 32.28°, and 36.85° while **complex 4** displayed peak at 2θ = 11.52°, 13.49°, 14.96°, 18.86°, 19.62° and 25.64°. The peaks at 2θ = 12.43°, 14.20°, 16.43°, 17.95°, 20.58°, 21.34°, 22.25°, 22.96°, 23.87°, 32.28°and 36.85° of the ligand **8** disappeared in the

complex **4** and new peaks appeared at 2θ = 11.52°, 14.96°, 19.62° and 25.64°**(figure 3.6c)**. This diffraction pattern confirms the formation of Cu(II) complex [9]. Similarly, in complex **6** new peaks were observed at 2θ = 10.49°, 19.92°, 25.34°, 26.25°, 35.01°, 38.91°, 42.8° and 44.73° which are in good agreement with previously reported oxovanadium V(IV) complexes **(figure 3.6d)** [38,39]. The X-ray diffraction patterns for ligand and complexes were different, which confirms the formation of **complex 4** and **6.**

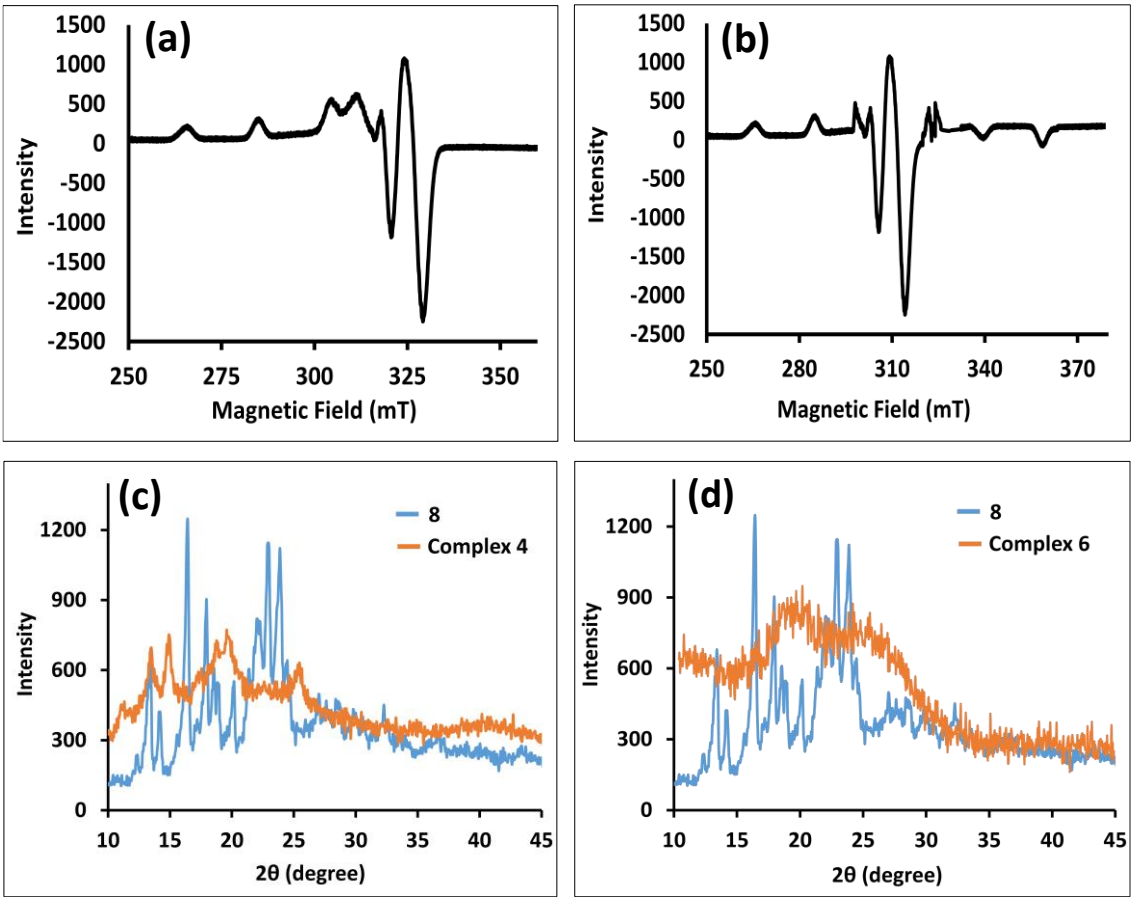

Figure 3.6 EPR spectra of (a) complex 1, (b) complex 6 and powder XRD pattern of (c) complex 4 and (d) complex 6 overlayed with ligand 8.

The synthesized Cu(II) and V(IV) complexes were air stable. The thermal stability of complexes was examined via thermogravimetric analysis (TGA). The TGA of **complexes 1-6** was carried out under a nitrogen atmosphere at elevated temperature with a heating rate of 10 ^{o}C min^{-1}. TGA plots of **complexes 1-6** are shown in **figure S3.13.**

For **complexes 1-5**, the first degradation occurred up to 160 ^{o}C can be attributed to the loss of lattice solvent [33]. The second degradation from 210 ^{o}C occurs due to the decomposition of the organic ligand from complexes [34]. In the case of **complex 6,** the

mass loss up to 150 ^{o}C occured due removal of lattice solvent and weakly coordinated H_2O. A second degradation stage after 150 ^{o}C was obtained due to pyrolysis of imidazole and an organic ligand. Thus, the TGA results indicated that all the complexes have good thermal stability.

3.2.4 DFT based theoretical study

Molecular orbitals (MOs) of highest occupied and lowest unoccupied are collectively referred to as frontier orbitals (FMOs). FMOs were calculated theoretically as they are important parameters for describing chemical behavior. The lowest unoccupied molecular orbitals (LUMO) are primarily electron acceptors and the highest unoccupied molecular orbitals (HOMO) are electron donors. The energy gap between the HOMO and LUMO correlates with the chemical stability of the molecules. Literature reports suggested that the compounds with a small energy gap possess higher chemical reactivity, low kinetic stability, and soft in nature, and vice versa for compounds that possess a high energy gap [40–42]. Details of frontier molecular orbitals along with the HOMO-LUMO energy gap are summarized in **table 3.5**, respectively. The energies of the Frontier molecular orbitals (FMOs) for **complexes 1-6** had negative values, indicating that the complexes were stable [43].

Table 3.5 Calculated frontier molecular orbital energies of complexes 1-6

Complex	LUMO	HOMO	ΔE (eV)
1	-3.34	-6.45	3.10
2	-3.22	-5.45	2.23
3	-3.25	-6.64	3.39
4	-3.03	-5.23	2.19
5	-3.67	-5.56	1.89
6	-2.54	-3.69	1.19

The metal-ligand bond lengths and bond angles are tabulated in **table 3.6** for **complexes 5** and **6**. The metal-ligand bond lengths and bond angles of the remaining complexes are provided in **table S3.1 (section 3.6)**.

Table 3.6 Metal ligand bond length and bond angle of complexes 5 and 6 under study obtained from geometry optimization

Complex 5			
Bond length (Å)	R(1,2)	Cu1- O2	1.9354
	R(1,40)	Cu1- O2	1.9464
	R(1,43)	Cu1-N43	2.0578
	R(1,5)	Cu1-N5	2.0472
Bond angle (°)	A(2,1,5)	O2-Cu1-N5	91.3379
	A(2,1,43)	O2-Cu1-N43	88.0869
	A(40,1,5)	O40-Cu1-N5	89.6101
	A(40,1,43)	O40-Cu1-N43	91.537
	A(2,1,40)	O2-Cu1-O40	179.6239
	A(5,1,43)	N5-Cu1-N43	181.1417
Complex 6			
Bond length (Å)	R(13,57)	O13-V57	1.9992
	R(59,57)	O59-V57	1.6101
	R(69,57)	N69-V57	2.1317
	R(15,57)	N15-V57	2.2015
Bond angle (°)	A(13,57,69)	O13-V57-N69	79.0648
	A(59,57,69)	O59-V57-N69	83.0692
	A(15,57,59)	N15-V57-O59	94.9665
	A(13,57,15)	O13-V57-N15	87.8228

The patterns of the HOMO and LUMO of **complexes 1-6** are displayed in **figure 3.7.** It was observed that the HOMO electron density is delocalized over the oxygen atom of the quinonoid ring of lawsone moiety in all the complexes and the LUMO electron density is localized on both benzenoid and quinonoid rings. In all cases, the HOMOs, as well as LUMOs, are not delocalized over the alkyl chains. The HOMO–LUMO gap for **complex 5** was observed to be 1.89eV, which indicated **complex 5** is the most chemically reactive among all other copper complexes. It was also observed that the chemical reactivity of the vanadium complex is more than that of all copper complexes as the HOMO-LUMO gap for the vanadium complex was found to be 1.19eV. The optimized structures of complexes are shown in **figure S3.14.**

Molecular electrostatic potential (MEP) is widely used as a reactivity map. MEP can display electrophilic sites (positive regions) and nucleophilic sites (negative regions) based on electrostatic potentials, which are represented by red and blue colors respectively [44,45]. The MEP diagram and electrostatic potentials of **complexes 1-6** are represented in **figure S3.15.** The red region can be observed near the O atoms of naphthoquinone ring of **complexes 1-6** and near the N atom of the pyridyl ring in **complexes 4** and **6** which symbolizes the acceptor site. The blue region near O atom of OH symbolizes the donor sites in **complexes 2**, **5,** and **6.** The blue region near the metal atom corresponding to the positive potential indicates it is a good candidate for attack by a nucleophile. These results confirm the formation of copper and vanadium complexes.

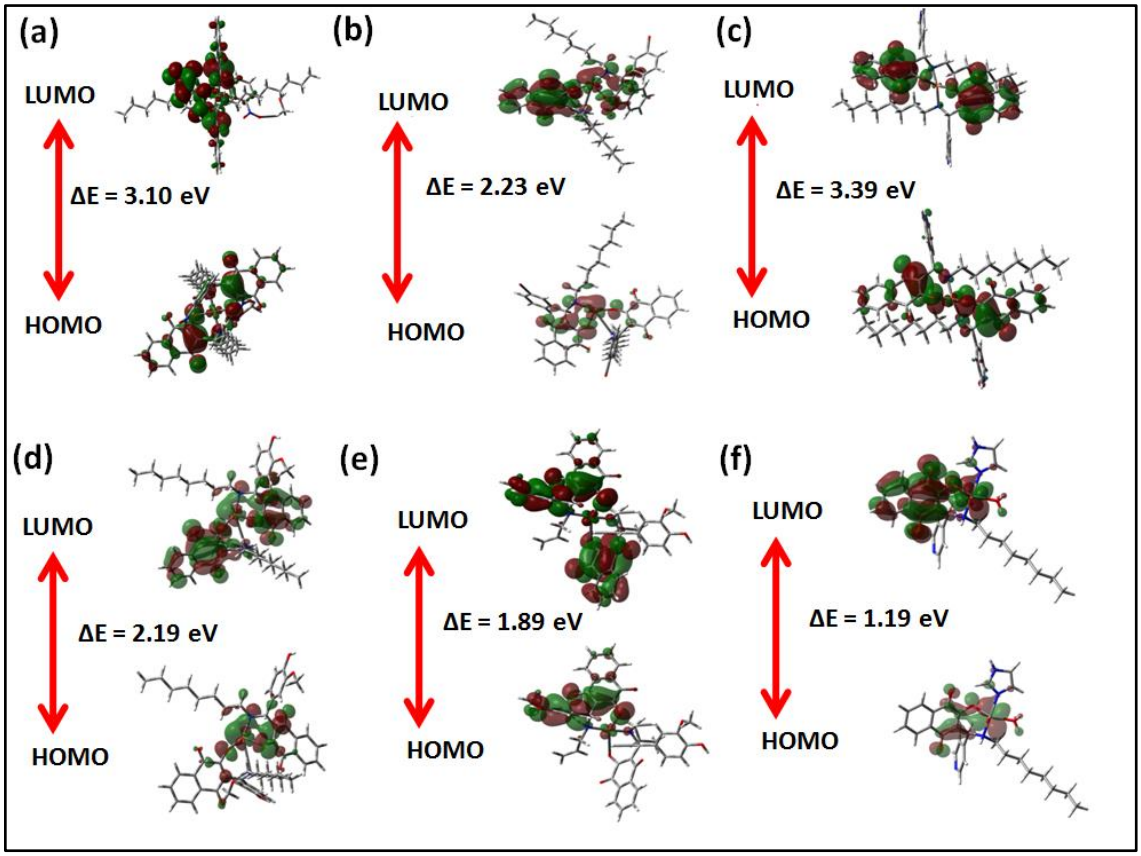

Figure 3.7 plots of the frontier molecular orbitals depicting the HOMO and LUMO structure with the energy level diagram of complex (a) 1 (b) 2 (c) 3 (d) 4 (e) 5, and (f) 6.

3.3 Biological studies

3.3.1 DNA binding studies

UV absorption spectroscopy is one of the most common techniques to determine the binding strength and modes of metal complexes toward DNA. The UV spectra of all the complexes (10^{-6} M prepared in DMSO) were recorded in the absence and presence of varying CT-DNA concentrations (at the ratio of 0 to 1.8) within. The appearance of hypochromism in absorption bands **(figure 3.8a,** and **3.8b)** is due to the partial occupation of π* orbitals of the ligands in the complexes which results in a decrease in transition probabilities *i.e.* intercalation mode and red-shift is the evidence of stabilization of double-helical DNA [46].

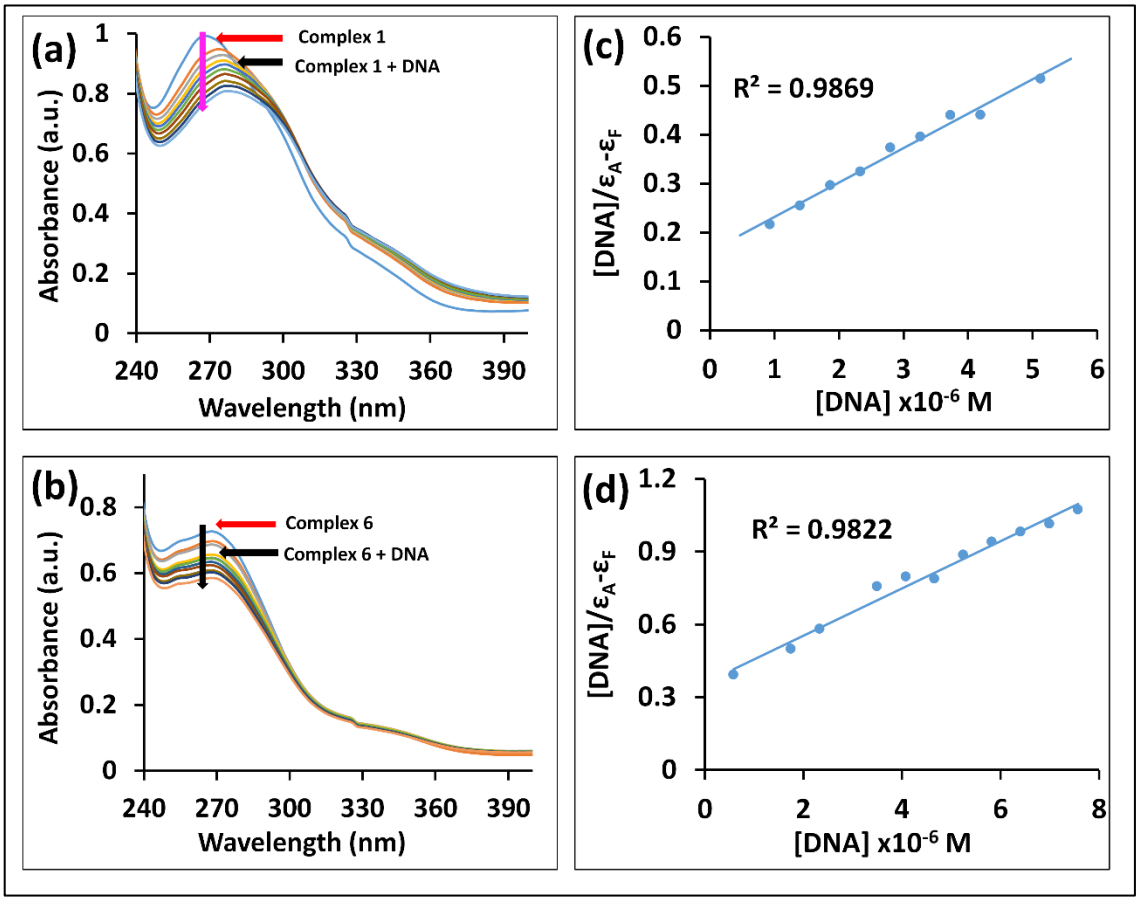

Figure 3.8 UV absorption spectra of (a) complex 1 and (b) complex 6 at increasing concentration of CT-DNA, the arrow shows a decrease in intensity upon the increasing concentration of the complexes. Plots of [DNA]/(εA-εf) vs. [DNA] of (c) complex 1 and (d) complex 6.

To quantitatively compare the binding affinity of complexes, the DNA binding constant (K_b) was calculated by a change in absorption spectra. A plot of [DNA]/(ε_A-ε_f) vs. [DNA] gave a slope 1/(ε_b-ε_f) and an intercept (1/K_b)(ε_b-ε_f), K_b is the ratio of the slope to intercept **(figure 3.8c and 3.8d)**. The binding constant (K_b) of complexes is calculated from Wolf –Shimer equation given below **(equation 3.1)** [47].

$$\frac{[DNA]}{(\varepsilon_A-\varepsilon_f)} = \frac{[DNA]}{(\varepsilon_b-\varepsilon_f)} + \frac{1}{K_b(\varepsilon_b-\varepsilon_f)} \quad \text{----------} \quad (3.1)$$

Where [DNA] is the concentration of DNA base pairs, ε_f, and ε_b are the extinction coefficient for the unbounded and free bounded form, and $\varepsilon_A = A_{obsd}/[compounds]$.

Figure 3.8a illustrates the intensity of free CT-DNA at λ_{max} = 268 nm decreases with an increased amount of **complex 1** and exhibits hypochromism with a small redshift (~ 8 nm). These prominent features indicate **complex 1** interacts with CT-DNA via intercalative mode. Similar behavior was observed for **complexes 2, 3 (figure S3.16a-3.16b),** and **6 (figure 6b).** While **complexes 4** and **5** showed hyperchromism **(figure S3.16c-S3.16d)**. It can be due to the groove binding of CT-DNA with complexes [48]. The binding constant K_b of complexes ranges from 10^5 to $10^6 M^{-1}$ **(table 3.7)** revealing the strong binding of complexes with DNA. The effect of size, shape, hydrophobicity, and electrolytic behavior of the metal complexes play significant roles in the binding of the complexes to DNA. It was observed that **complexes 4** and **5** showed high binding affinity due to strong lone pair-π interaction that has been suggested to stabilize DNA and protein structure, which contributes to the excellent binding affinity towards DNA via intercalative and groove binding mode [48,49]. **Complex 6** showed good binding affinity due to positive charge (+2) which may result in electrostatic interactions between a positively charged complex unit with the negatively charged phosphate backbone of CT-DNA double helix [50]. The high binding affinity of **complexes 5** and **6** to DNA can be attributed to their higher chemical reactivity. They have a low energy difference between HOMO-LUMO. Another important factor that was considered to investigate the nature of complexes towards DNA *i.e.* spontaneity/non-spontaneity. Gibb's free energy (ΔG) was calculated according to **equation 3.2**

$$\Delta G^\circ = -RTlnK_b \quad \text{----------} \quad (3.2)$$

Where R = 8.314 $JK^{-1}mol^{-1}$ and T = 298 K. The observed negative values of ΔG **(table 3.7)** suggested that the binding process of complexes towards DNA was energetically favorable and spontaneous [51].

Table 3.7 K_b and *Ksv* values of complexes 1-6

Complex	K_b (M^{-1})	*Ksv* (M^{-1})	ΔG° (KJ mol^{-1})	λ shift (nm)
1	4.36×10^5	6.6×10^3	-32.175	8
2	5.38×10^5	5.0×10^3	-32.695	8
3	1.72×10^5	6.3×10^3	-29.874	7
4	3.57×10^6	8.3×10^3	-37.382	2
5	1.75×10^6	1.02×10^4	-35.621	2
6	2.70×10^5	2.37×10^4	-30.984	-

To further elucidate the exact binding mode of the complexes with CT DNA, a competitive binding study was carried out by quenching experiment with the use of fluorescence spectroscopy. The emission spectra of DNA-EB (λ_{ex} = 546 nm, λ_{em} = 612 nm) in the absence and presence of the increasing amount of complexes (at ratios of 0-2.0) were recorded. With increasing concentration of complexes, a considerable decrease in intensity of DNA-EB emission band at 612 nm was observed as shown in **figure 3.9.** The emission band exhibits a significant hypochromism effect that may be attributed to the π -π* stacking interaction and stabilization of double-helical DNA. This observation implies that all **complexes 1-6** have a great tendency to displace EB from the DNA-EB conjugate and strongly bind with DNA via intercalative or groove binding mode [52]. The displacement of bound EB and quenching of fluorescence proves complexes interact with DNA more strongly via intercalation. It might be due to the planar structure of complexes as proven by single crystal XRD and DFT study [53]. The quenching ability of DNA-EB conjugates by complexes was analyzed according to Stern Volmer **equation 3.3.**

$$\frac{I_0}{I} = 1 + K_{SV}[Q] \quad \text{----------} \quad (3.3)$$

Where I_0 and I represent the emission intensities of DNA-EB conjugates in the absence and presence of quencher [Q] (i.e **complexes 1-6**) respectively. K_{sv} is Stern Volmer quenching constant and it is obtained by the slope of linear plots between I_0/I *versus* [Q] **(figure S3.17)**. The Stern-Volmer quenching constant K_{sv} values are given in **table 3.7** and following the order **complex 6 > complex 5 >complex 4 > complex 1 > complex 3**

> **complex 2**. This order suggests that oxovanadium complex **6** and Cu(II) complex **5** exhibit the best results. This might be due to the low HOMO-LUMO gap as shown in DFT study **(figure 5, table 5)** and the presence of higher positive charge (+2) in oxovanadium complex **6** and allylic group in complex **5** [48,49]**.** The magnitude of the binding constant value indicated medium to strong binding strength of complexes with CT-DNA [52]. The titration plot of the remaining complexes is provided in **section 3.6 (figure S3.18a-S3.18d)**.

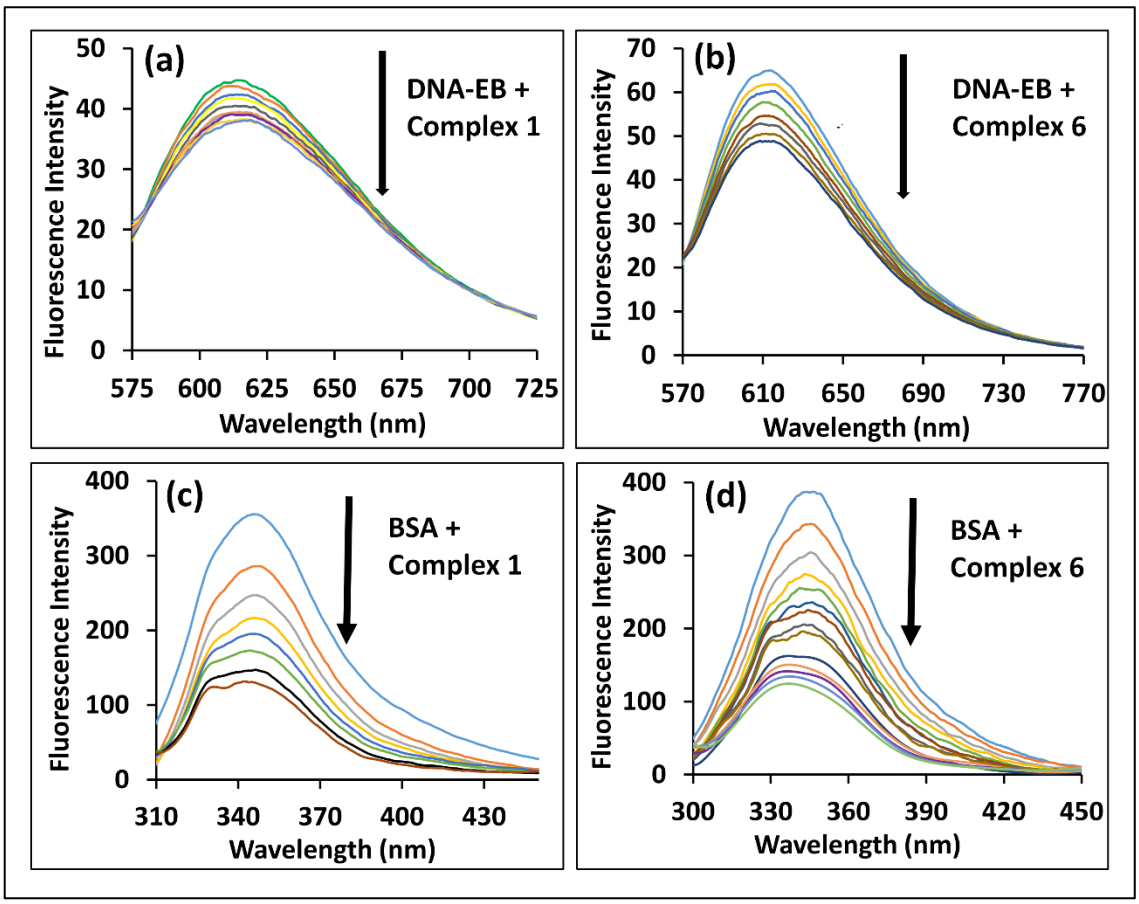

Figure 3.9 Plot of fluorescence emission intensity I *versus* wavelength λ of CT-DNA-EB and BSA at increasing concentrations of complex 1 (a, c), and complex 6 (b, d) respectively.

3.3.2 BSA binding studies

Albumin is the most abundant protein in vertebrates. Studies on the binding affinity and mechanism of interaction of small molecules with serum albumin are crucial. BSA was selected as a target protein in our case due to its structural similarity with human serum albumin, easy availability, and low cost [54]. The addition of an increasing concentration

of **complex 1** (a ratio of 0-5.0) to a solution of BSA leads to a decrease in fluorescence emission at 346 nm as shown in **figure 3.9c** indicating the formation of a complex-BSA system. A similar trend was also observed for **complexes 2-5 (figure S319a-S3.19d).**

The fluorescence quenching could be occurred by dynamic quenching and static quenching. The former is a collisional process (the fluorophore and the quencher interact in the excited state), while the latter is related to the formation of a non-fluorescent complex by the fluorophore and quencher. This quenching effect was also analyzed by the Stern-Volmer **equation 3.3.** For static quenching interaction, the apparent binding constant K_a and the number of binding sites n could be obtained from the Scatchard equation: $\log((I_0\text{-}I)/I) = \log Ka + n\log[Q]$ [55,56]. The plot of $\log[I_0\text{-}I/I]$ versus $\log[Q]$ for all the **complexes 1-6 is** linear as shown in **figure S3.20a.** The binding constant (K_a) and the number of binding sites per albumin (n) have been obtained from the intercept and slope respectively **(table 3.8).** The values of n approximately range between 1 to 1.5, which indicated that there was only one class of independent binding sites for **complexes 1-5. Complex 5**, **4,** and **6** showed the highest level of BSA binding among all complexes **(table 3.8).** The higher binding affinity of **complexes 5, 4,** and **6** towards BSA could be explained in terms of the planarity of ligands coordinated to the metal centers. The oxovanadium **complex 6** showed higher binding to BSA compared to copper **complexes 1-3** may be due to the static and dynamic quenching mechanism[57].

Table 3.8 K_a and Ksv values of complexes 1-6

Complex	K_a (M^{-1})	Ksv (M^{-1})	n
1	3.103×10^5	2.828×10^5	1.01
2	2.4677×10^5	2.102×10^5	1.019
3	1.43×10^5	1.539×10^5	0.9962
4	5.0384×10^6	3.426×10^5	1.2463
5	15.790×10^7	3.497×10^5	1.5743
6	1.37×10^6	1.562×10^5	1.19

The values of the Stern Volmer quenching constant K_{sv} obtained from the plot of $[I_0/I]$ versus $[Q]$ for the complexes interacting with BSA are in order of 1.56 to 3.49 ($\times 10^5$ M^{-1}). The Stern–Volmer plot for the quenching of BSA fluorescence by **complexes 1-6** is shown in **figure S3.20b**. The n value suggests that there is one binding site available on

the protein. In addition, the linear nature of the double logarithm plot indicates that only one of the tryptophan residues on the protein is interacting with the complexes.

All spectroscopic method clearly proved that the overall order of interaction is **complex 5 > complex 4 > complex 6 > complex 1 > complex 3 > complex 2. Complex 5** exhibits the strongest binding with both DNA and BSA. This phenomenon may be related to the presence of allylic group, which provides planarity to the metal center of the complex and also act as an electron donor group. It may assist the respective interaction between complex and either DNA or protein. A similar phenomenon was also observed in other complexes [52,54].

3.3.3 Cytotoxicity

Complexes 3, 4, 5, and **6** were selected for in vitro cytotoxicity study on HepG2 cell lines (Human liver cancer cells) based on results obtained from DFT and DNA/BSA binding study. All the compounds were screened (at 1, 2, 3, 4, 5, and 10 μM concentrations) for 48 h for cell viability (by MTT) assay and IC_{50} values were obtained [3]. The plot of % viability *vs* concentration of compound obtained is shown in **figure 3.10(I). Complex 3** recorded a moderate (about 8%) cytotoxicity at 5 μM dose. In contrast, **complex 6** had recorded a sharp decline in cell viability at 3 μM of concentration. **Complexes 4,** and **5** accounted for approximately 50% decrement in cell viability at 3 μM concentration. The cytotoxicity of complexes in descending order are **complex 6 > complex 5 > complex 4 > complex 3** whereas; their IC_{50} values are shown in **table 3.9.**

Table 3.9 IC_{50} values of Complexes

Complex	3	4	5	6
IC_{50} (μM)	5.46 (37.19)	3.325 (4.56)	3.32 (389.54)	2.71 (4.56)

Herein, it is interesting to note that the obtained cytotoxic values are more effective than their precursor ligands (mentioned in parenthesis)[3], and is comparable with IC_{50} value of cisplatin (15.9 μM on HepG2 cells) [58].

3.3.4 Acridine Orange Ethidium Bromide (AO/EB) Staining

The early apoptosis induced by complexes was confirmed by AO/EB staining. It is well known that early apoptosis is close to a physiological phenomenon, such as progressive

contraction in cell volume while tumor cell necrosis could induce rupture into membranes, leakage of cellular space into extracellular space, and results in inflammation in normal cells. Green stained unfragmented nuclei were observed in control cells, indicating non-apoptotic cellular status. Whereas, the treated cells were observed with green fragmented nuclei. EB stains the cells with spoor membrane integrity. Cells in **complex 3** observed higher red fluoresce, as compared to others, witnessing necrotic cell death. However, the cells in **complexes 4** and **5** showed higher nuclear condensation implying towards apoptotic cell death. Cells dosed with **complex 6** showed higher nuclear condensation and a lower amount of orange fluorescence implying towards necrotic cell death. AO/EB staining for **complexes 3-6 is** shown in **figure 3.10(II).**

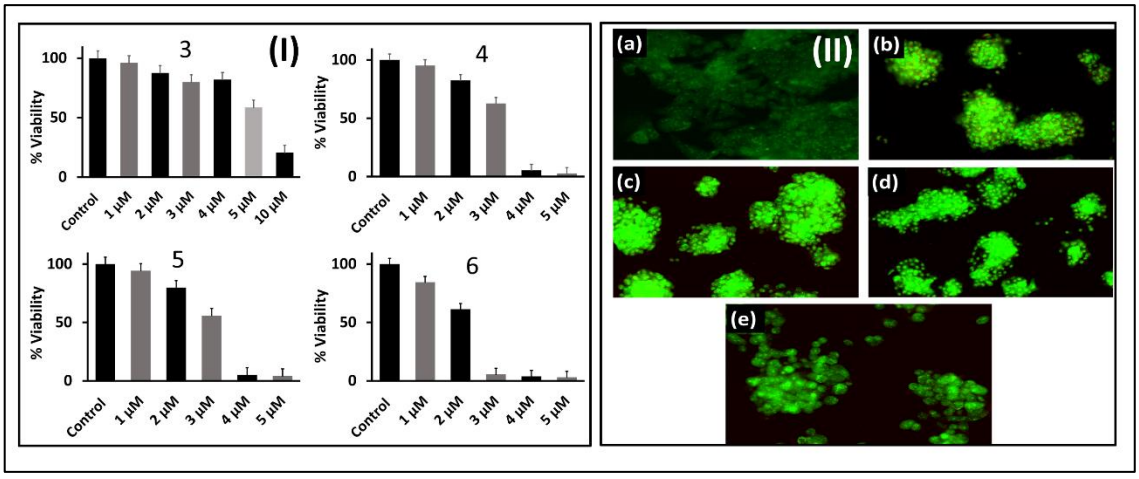

Figure 3.10 (I) The plot of % viability *vs* concentration of compound obtained from MTT assay of complexes and (II) AO/EB staining for the complexes (a) Control (b) 3 (c) 4 (d) 5 and (e) 6 at their IC_{50} values for 48 h.

3.4 Experimental

3.4.1 Material and methods

Lawsone, vanadyl sulfate, aldehydes, and amines were purchased from Sigma-Aldrich, Mumbai, India and used as received. Copper acetate was purchased from Loba Chemie, India. Calf thymus DNA (CT-DNA), Trisodium citrate ($Na_3C_6H_5O_7$), Ethidium Bromide (EB), and bovine serum albumin (BSA) were procured from Sisco Research Laboratory (SRL) Mumbai, India. HepG2 cell line was procured from National Center for Cell Science (NCCS) Pune, India. The buffer solution was

prepared by mixing 5 mM trisodium citrate and 50 mM NaCl in doubly distilled water and NaOH solution was used to adjust pH to 7.4.

The description of instruments used for FTIR, NMR, elemental, and Mass analysis is depicted in **chapter 2 (section 2.3.1)**. ESR spectra were recorded using JOEL JES-FA-200 ESR spectrometer operating with X-band (9.6 GHz) microwave at liquid nitrogen temperature in a suitable solvent. Thermogravimetric Analysis (TGA) of ligands and complexes were performed TG–DTA 6300 INCARP EXSTAR 6000 at a heating rate of 10°C/min in the temperature range of 30–500°C, nitrogen atmosphere was maintained throughout the measurement. UV-Visible spectra were recorded on Perkin Elmer Lambda-35 dual-beam spectrophotometer and Fluorescence spectra were recorded in solution on JASCO FP-6300 fluorescence spectrophotometer. Powder XRD was recorded on Bruker D2-Phased instrument with Lynux-eye detector.

3.4.2 General procedure for the synthesis of complexes 1-6

Copper acetate (0.5 mmol) dissolved in methanol (15 mL) was added dropwise to the solution of ligand (1 mmol) in methanol (20 mL). The resulting brownish reaction mixture was then refluxed for 5 h at 65 °C, with continuous stirring, after which the solution was allowed to cool to room temperature. The light green to the brownish crystalline product was filtered and given washing with hot water and dried under vacuum. The general schematic for synthesis is shown in **scheme 3.1(a)**.

Complex 1

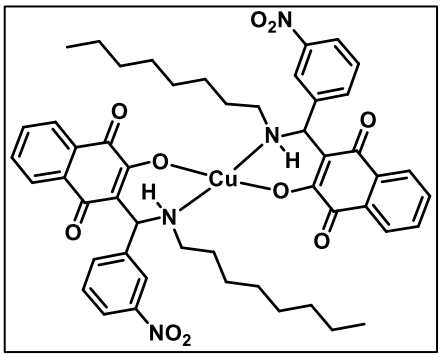

Green crystalline solid; Yield: 81%; M.P: 182-184^{o}C

For $C_{50}H_{54}CuN_4O_{10}$: Anal. Calculated %: C, 64.26; H, 5.82; N, 6.0. Found %: C, 64.52; H, 5.45; N, 5.87 **IR (KBr) cm^{-1}**: 3434 (N-H), 3065 (=C-H), 2926 (C-H), 1676 (C=O), 1590 (N=O), 1549 (δ N-H), 1376 (N=O), 1273 (C-O), 523 (Cu-N), 431 (Cu-O).

UV-Vis ($CHCl_3$) λ/nm, (log ε): 266 (4.58), 422 (3.42), 590 (2.08).**Molar conductance:** 6.67 S cm^2 mol^{-1}

Complex 2

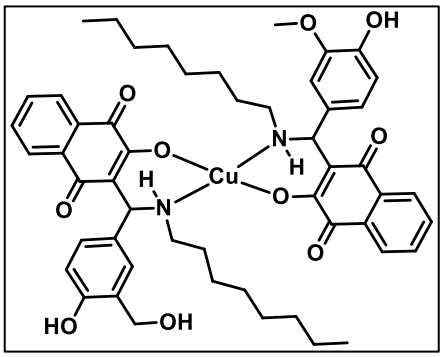

Brown crystalline solid; Yield: 76%; M.P: 190-192 ºC

For $C_{52}H_{60}CuN_2O_6$: Anal. Calculated %: C, 66.68; H, 6.46; N, 2.99. Found %: C, 66.67; H, 6.42; N, 3.05 **IR (KBr) cm^{-1}**: 3462 (N-H), 3138 (=C-H), 2928(C-H), 1678 (C=O), 1544 (δ N-H), 1275 (C-O), 1089 (C-N), 522 (Cu-N), 429 (Cu-O) **(figure S3.2), UV-Vis ($CHCl_3$) λ/nm, (log ε):** 268 (4.51), 424 (3.48), 594 (2.16). **Molar conductance:** 18.74 S cm^2 mol^{-1}

Complex 3

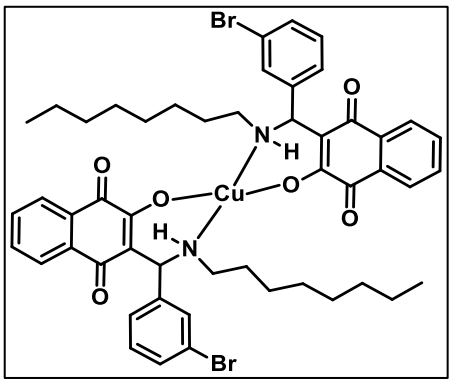

Brown crystalline solid; Yield: 76%; M.P: 190-192 ºC

For $C_{50}H_{54}Br_2CuN_2O_6$: Anal. Calculated %: C, 59.91; H, 5.43; N, 2.79. Found %: C, 60.02; H, 5.51; N, 2.75.**IR (KBr) cm^{-1}**: 3462 (N-H), 3176 (=C-H), 2958 (C-H), 2926 (C-H), 1673 (C=O), 1620 (C=C), 1545 (δ N-H), 1273 (C-O), 703 (C-Br), 519 (Cu-N), 431 (Cu-O) **(figure S3.3), UV-Vis ($CHCl_3$) λ/nm, (log ε):** 428 (3.52), 586 (2.05). **Molar conductance:** 6.26 S cm^2 mol^{-1}

Complex 4

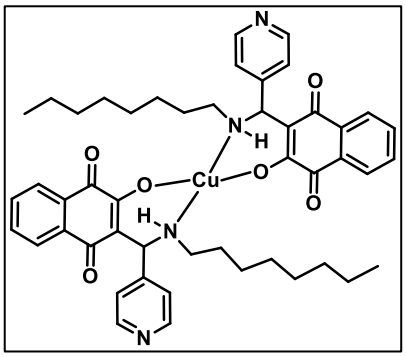

Green crystalline solid; Yield: 81%; M.P: 178-182 ^{o}C

For $C_{48}H_{54}CuN_4O_6$: Anal. Calculated %: C, 68.11; H, 6.43; N, 6.62. Found %: C,68.15;H,6.45;N,2.75.**IR (KBr) cm^{-1}**: 3443 (N-H), 3070 (=C-H), 2960(C-H), 2853(C-H), 1678 (C=O), 1591 (C=N), 1547 (δ N-H), 1272 (C-O), 1064 (C-N), 566 (Cu-N), 430 (Cu-O) **(figure S3.4), UV-Vis ($CHCl_3$) λ/nm, (log ε):** 278 (4.22), 435 (3.78), 681 (2.17).**Molar conductance:** 17.95 S cm^2 mol^{-1}

Complex 5

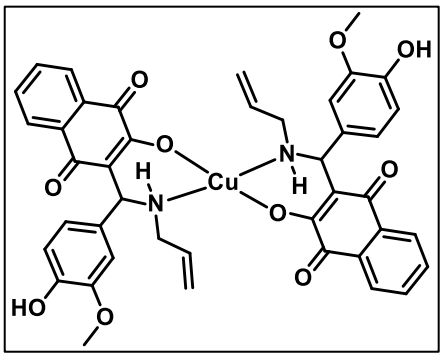

Brown crystalline solid; Yield: 70%; M.P: 188-190 ^{o}C

For $C_{42}H_{36}CuN_2O_{10}$: Anal. Calculated %: C, 63.67; H, 4.58; N, 3.54. Found %: C, 63.70; H, 4.52; N, 6.62 **IR (KBr) cm^{-1}**: 3491 (N-H), 2924 (C-H), 2854 (C-H), 1675 (C=O), 1547 (δ N-H), 1280 (C-O), 1064 (C-N), 523 (Cu-N), 434 (Cu-O) **(figure S3.5), UV-Vis ($CHCl_3$) λ/nm, (log ε):** 264 (4.67), 436 (3.85), 680 (2.32). **Molar conductance:** 15.44 S cm^2 mol^{-1}

Complex 6

Vanadyl sulfate pentahydrate (1 mmol) dissolved in aqueous methanol (10 mL) was added dropwise to a suspension of ligand **8** (1 mmol) in methanol (15 mL) and refluxed for 2 h. Then imidazole (1 mmol) dissolved in methanol (5 mL) was added and continued reflux further 1 h. The color of the solution changed to brown color. The resulting brown

solid was filtered, washed with methanol and dried under vacuum. The schematic for the synthesis of **complex 6** is shown in **scheme 3.1(b).**

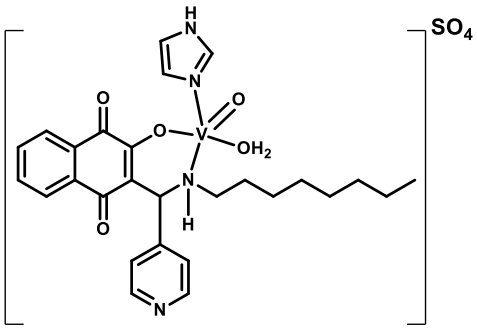

Brown powder; Yield: 65%; M.P: >300 ^{o}C

For $C_{27}H_{33}VN_4O_9S$: Anal. Calculated %: C, 50.62; H, 5.19; N, 8.75. Found %: C,51.08; H,5.10; N, 8.79 **IR (KBr) cm^{-1}**: 3472 (N-H), 3147 (C-H), 2932 (C-H), 1636 (C=O), 1591 (C=N), 1564 (δ N-H), 1360 (C-N), 1286 (C-O),974 (V=O), 552 (V-N), 447 (V-O) **(figure S3.6), UV-Vis ($CHCl_3$) λ/nm, (log ε):** 436 (0.535), 838 (0.22). **Molar conductance:** 114 S cm^2 mol^{-1}

3.5.3 X-Ray structure determination

The crystals suitable for single crystal X-ray analysis were grown by slow evaporation of complex solution in methanol at room temperature. The single crystal determination of **complex 1** was carried out on Bruker CCD area diffractometer with graphite monochromatized MoKα radiation (λ = 0.071073 nm) at 293 K. The mercury software package was used for ORTEP view of complex **1**. The structure was solved by the direct method using Olex2 [59]. The structure was refined on F2 with a ShelXL refinement package using least square minimization [60]. All hydrogen atoms were included at the geometrically calculated position and all non-hydrogen atoms were refined anisotropically **[CCDC No: 2092471]**.

3.5.4 Computational Studies

Theoretical calculations were carried out using Gaussian 16 software program. Density functional theory (DFT) calculation was assigned to optimize the geometry of the complexes using B3LYP/6-311G (d,p) and LanL2DZ basis sets. Frontier molecular orbitals(FMO), the HOMO-LUMO energy gap of the complexes (1-6), theoretical IR frequencies and Molecular electrostatic potential(MEP) were visualized with the aid of the Gauss View visualization program.

3.5.5 DNA Binding Experiments

DNA is considered as the primary biological target on numerous antitumor drugs, a series of spectroscopic tools have been employed for the determination of in vitro binding modes and binding strength of the complexes towards DNA. All the experiments were performed in buffer solution (5 mM trisodium citrate and 50 mM NaCl at pH 7.4) at room temperature (rt).

UV-visible spectroscopy is one of the popular method for evaluating the interaction of compounds with CT-DNA and to investigate possible binding modes of metal complexes towards DNA. The stock solution of CT-DNA was prepared in a buffer and stored at 4^{o}C while the stock solutions of complexes were prepared in DMSO. The concentration of CT DNA solution was determined from its absorption intensity at 260 nm by the use of the molar extinction coefficient (e) = 6600 M^{-1} cm^{-1}. The absorbance ratio at 260 nm and 280 nm was found to be 1.8–1.9 which suggests a negligible protein-contamination of CT DNA. The absorption studies were performed with a fixed concentration of complexes (20 μL/10μL) while varying the concentration of CT-DNA (0-60μL) in 5 mM Tri sodium citrate/ 50 mM NaCl buffer, pH 7.4. The solution of CT-DNA was at different ratios to both the compound and reference solution during absorption measurement to eliminate the absorbance of CT-DNA itself in spectra [61].

Fluorescence spectroscopy is an important tool as well as the most reliable technique to examine the competitive binding study of complexes with DNA and to determine whether the compound can replace EB from DNA-EB complex.

The DNA-EB complex was prepared by adding 100 μL of each EB (1 mM) and DNA in 2.8 mL tris buffer in the cuvette. The binding mode of complexes with CT-DNA was studied by adding 2.5 or 5μL of a complex solution (prepared in DMSO) step by step into the solution of the DNA-EB complex. The influence of the addition of complex in DNA-EB complex was recorded by fluorescence emission spectra. The fluorescence intensities of EB bound to CT-DNA were measured at 618 nm (580 nm excitation) after the addition of different complexes at different ratios.

3.5.6 BSA binding experiments

A protein binding study was carried out by quenching the tryptophan fluorescence residue of BSA. The fluorescence spectra were recorded at room temperature from 300

nm to 600 nm at the excitation wavelength of 296 nm. The quenching of the fluorescence intensity of the tryptophan residues of BSA was observed in the presence of increasing concentrations of **complexes 1-6** (5 mM Tri sodium citrate/ 50 mM NaCl buffer, pH 7.4) at 346 nm. The Stern Volmer equation and graphs were plotted and used to study the interaction of quencher with BSA [44,62].

3.5.7 Cell viability assay (MTT assay)

IC_{50} values of cell proliferation for synthesized compounds were determined using MTT assay following the same procedure as described in **chapter 2**. HepG2 cells (10^4 cells per well) were seeded in 96-well culture plates in 10% DMEM. Dilutions of the compounds were prepared in incomplete DMEM media. Dosing was done at about 70% confluency. After 48h incubation 3-(4, 5-dimethylthiazol-2-yl)-2,5-diphenyl tetrazolium bromide (MTT; 5 mg/ml) was added for 4h. At the end of incubation, MTT was removed from the wells and 150 μL/well of DMSO was added and incubated till formazan crystals dissolved completely. Absorbance was measured on Synergy HTX multimode reader at 570 nm. Statistical analysis was carried out using one way ANOVA test. IC_{50} values for the compounds were determined using MTT assay

3.5.8 Assessment of apoptosis (Acridine Orange Ethidium Bromide (AO/EB) staining)

HepG2 cells were seeded in 96 well plate. At about 70% confluency the cells were dosed with compounds at their IC_{50} concentration in an incomplete DMEM media and incubated for 48h. Cells were washed with 1x PBS and 5 μM of AO/EB stain was added for about 10 min. The stain was removed and cells were washed with 1x PBS twice and imaging was done on Floid Imaging Station using red and green fluorescent filters.

3.5 Conclusion

In conclusion, some copper and vanadium complexes were synthesized from bioactive lawsone based ligands and tested for anticancer activity. Single crystal X-ray diffraction analysis revealed that complex containing copper atom **(complex 1),** is in slightly distorted square planar geometry. The geometrical parameters of **complex 1** obtained by XRD correlated with theoretical DFT studies. Some important parameters such as bond length, bond angle, HUMO and LUMO energy gap (ΔE) were also determined using theoretical DFT study. The CT-DNA and BSA binding of complexes were studied by

employing UV-visible and fluorescence spectroscopy. The spectroscopic data have confirmed that all complexes efficiently bind with CT-DNA via intercalative or groove binding mode. The **complex 4** exhibits the highest binding affinity with binding constant K_b = 3.57 x 10^6 M^{-1} for CT-DNA. The results of BSA binding study revealed that quenching of proteins occurs in a static mode. It is noteworthy that **complex 5** exhibited higher protein binding affinity than other complexes (K_a = 15.790 x 10^7 M^{-1}), whereas vanadium **complex 6** also has higher protein binding affinity compared to copper **complexes 1-3** (K_a = 1.37 x 10^6 M^{-1}). A theoretical investigation using DFT allows rationalization of experimental findings. A significant cytotoxic potential of **complexes 3-6** was recorded against HepG2 cell line (by MTT assay) wherein; the findings are in agreement with experimental results and comparable to known anticancer drug cisplatin. A prominent green fluorescence following AO/EB staining in treated HepG2 cells implies to trigger of an apoptotic cascade that also corroborates with the observed cytotoxicity. The biological studies imply that these new compounds could serve as a non-platinum anticancer compound with remarkable cytotoxic effectiveness.

Based on results obtained by copper and vanadium complexes derived from bidentate mannich base ligands, it was proposed to synthesize tridentate mannich base as ligand and its metal complexes, which are discussed in chapter 4.

3.6 Spectra and Figures

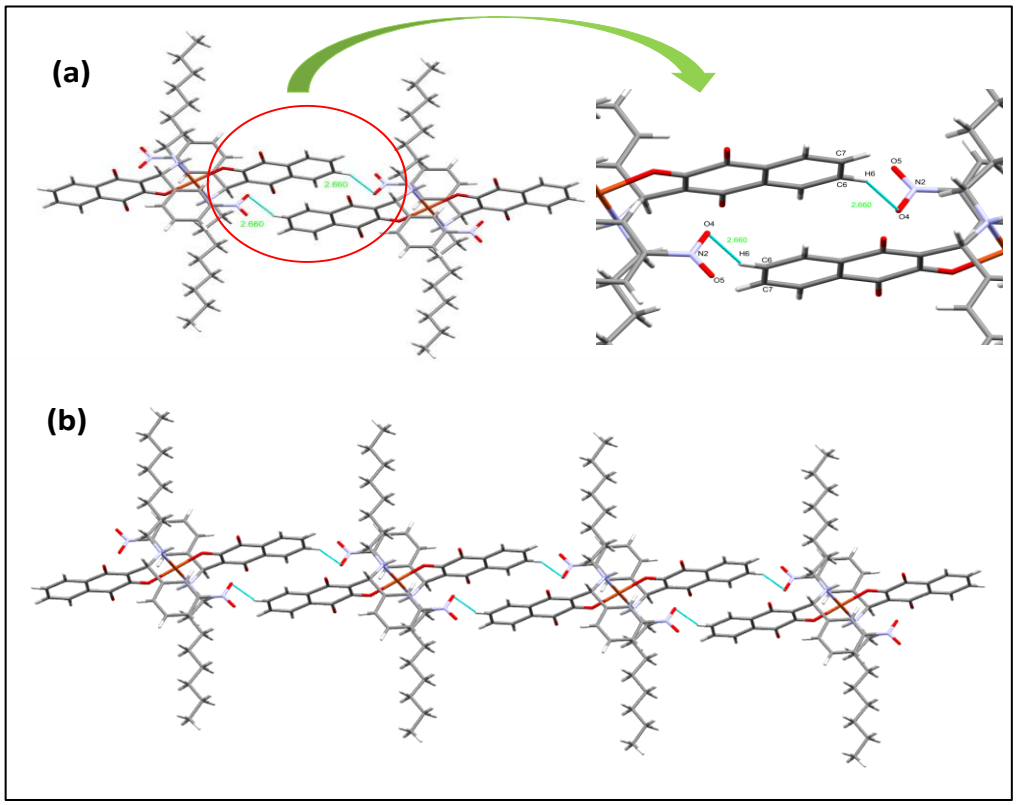

Figure S3.1 (a) Intermolecular hydrogen bonding interaction and (b) layer structure along *b* crystallographic axis in crystal lattice of complex

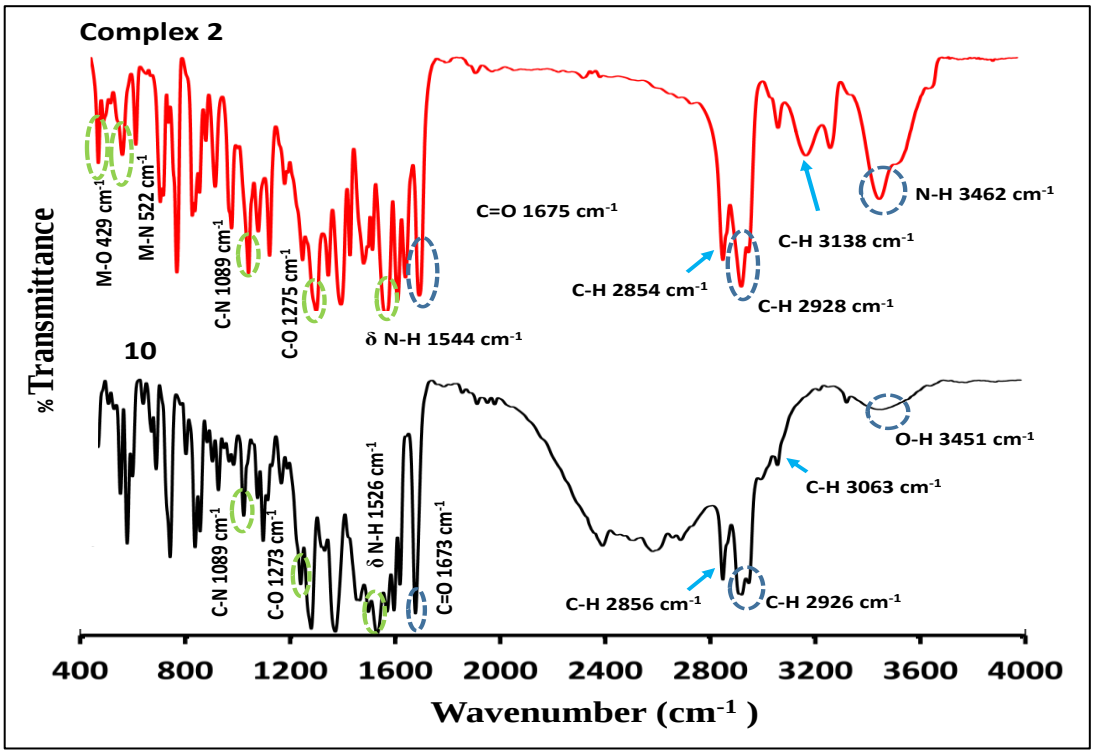

Figure S3.2 FT-IR spectra of complex 2

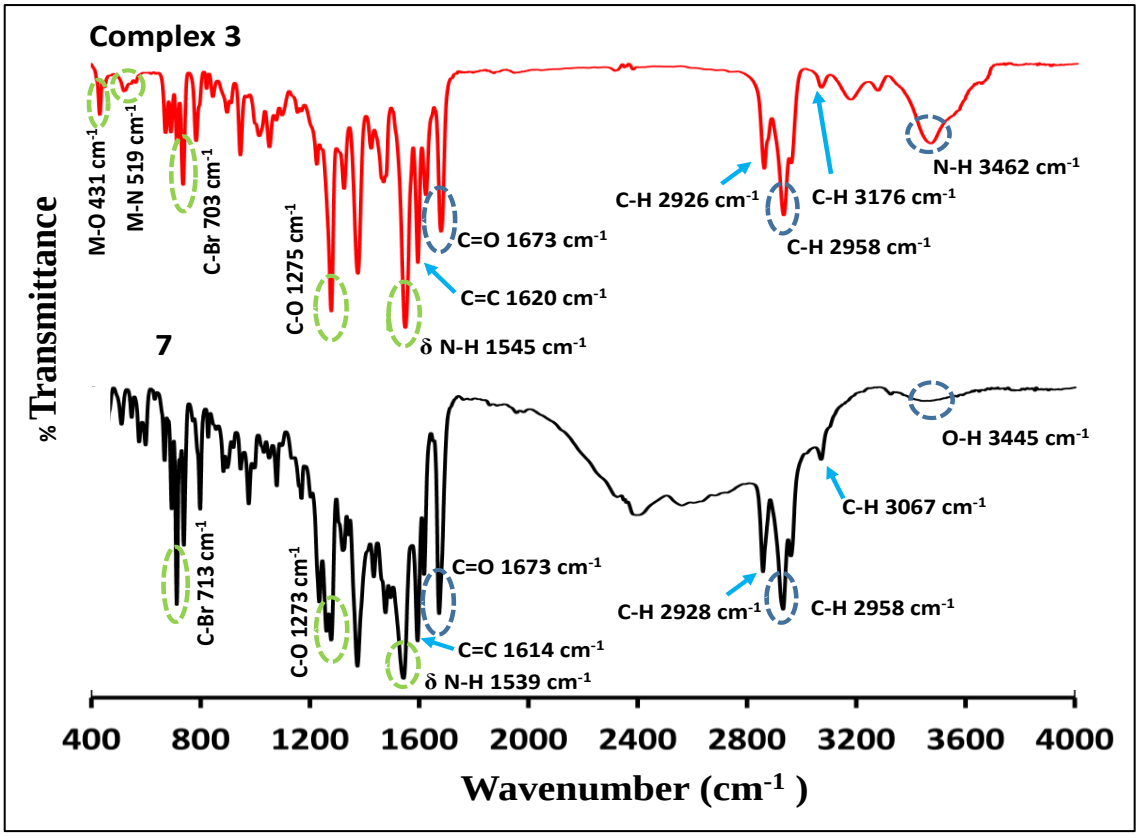

Figure S3.3 FT-IR spectra of complex 3

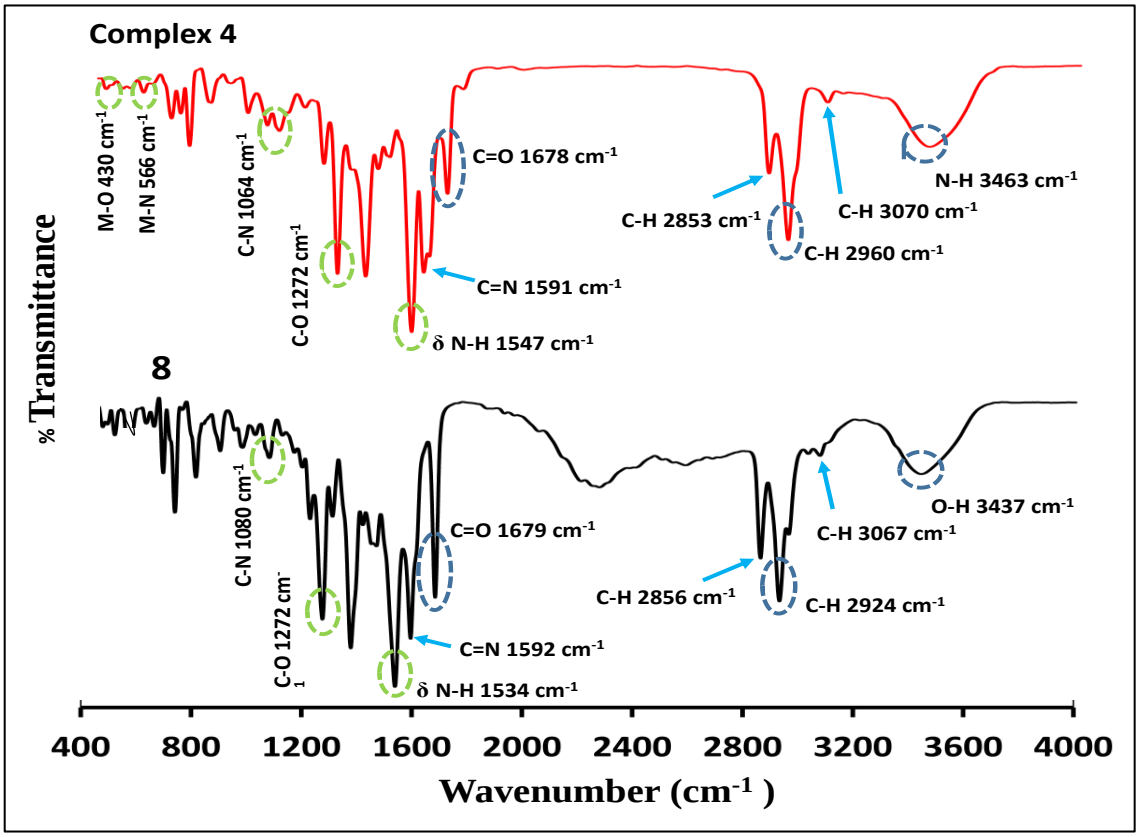

Figure S3.4 FT-IR spectra of complex 4

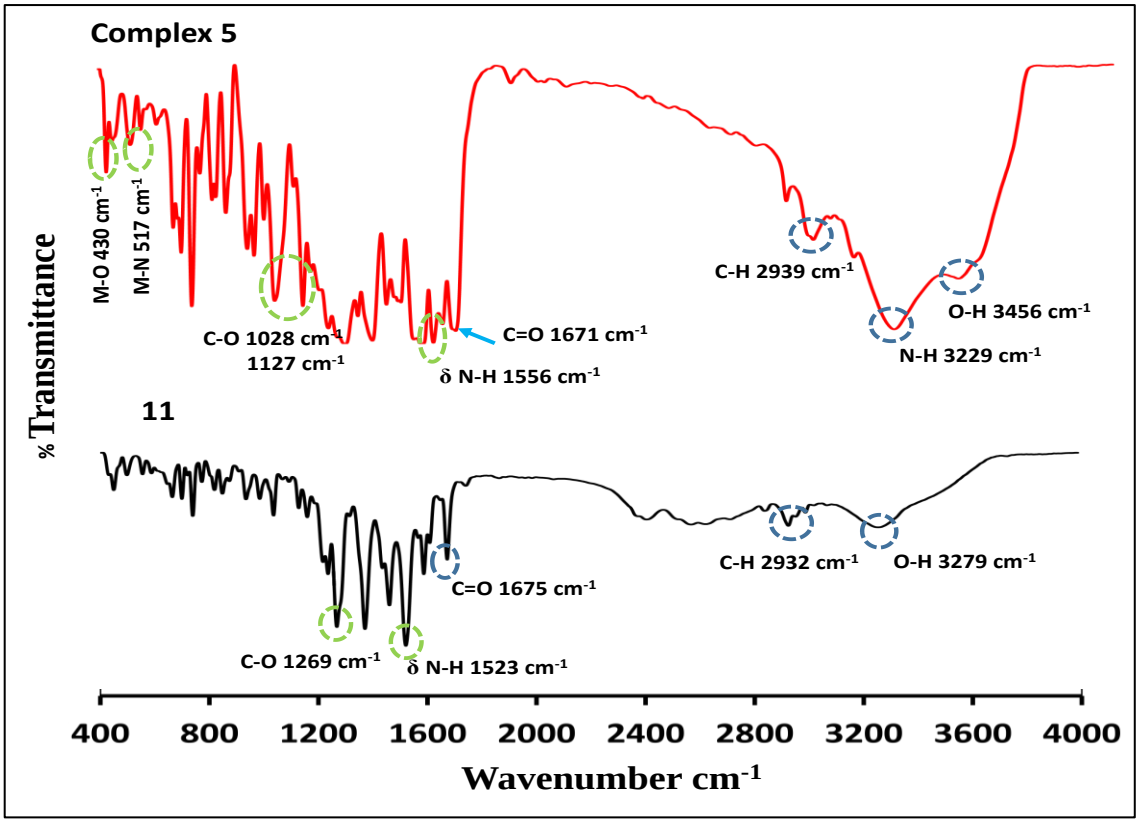

Figure S3.5 FT-IR spectra of complex 5

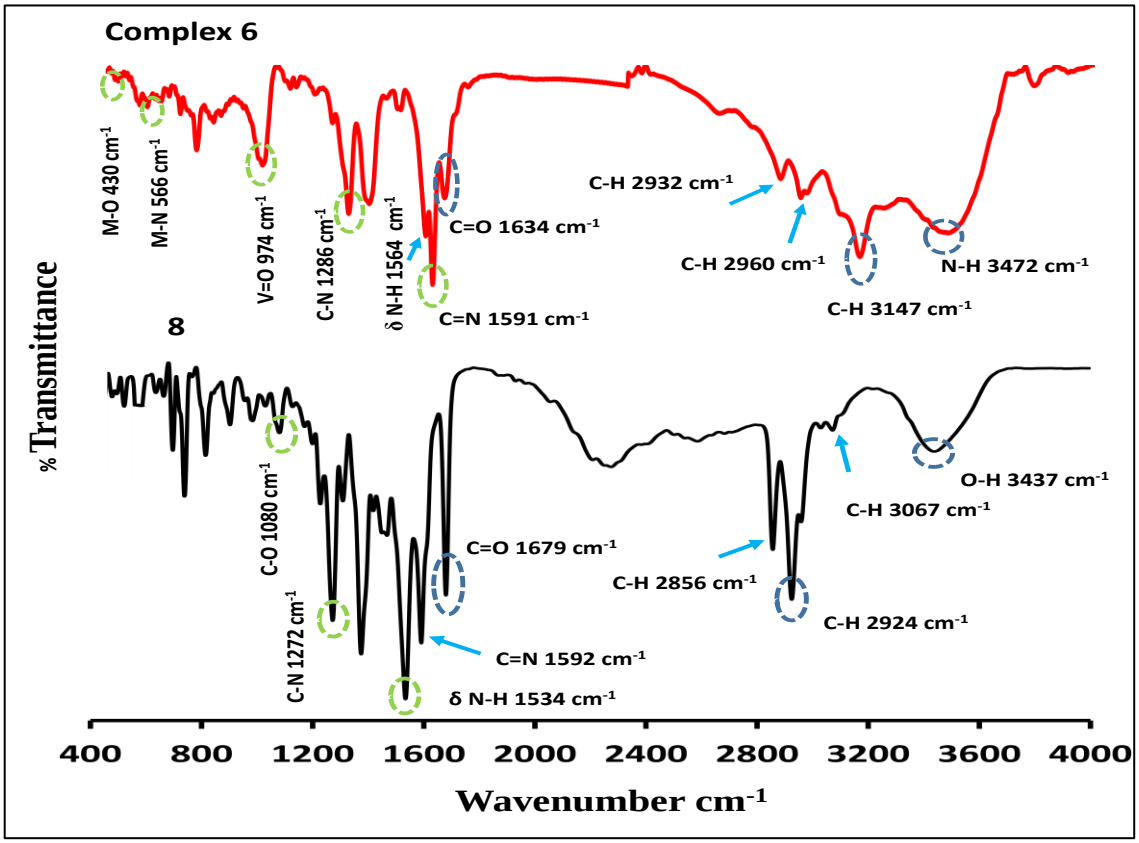

Figure S3.6 FT-IR spectra of complex 6

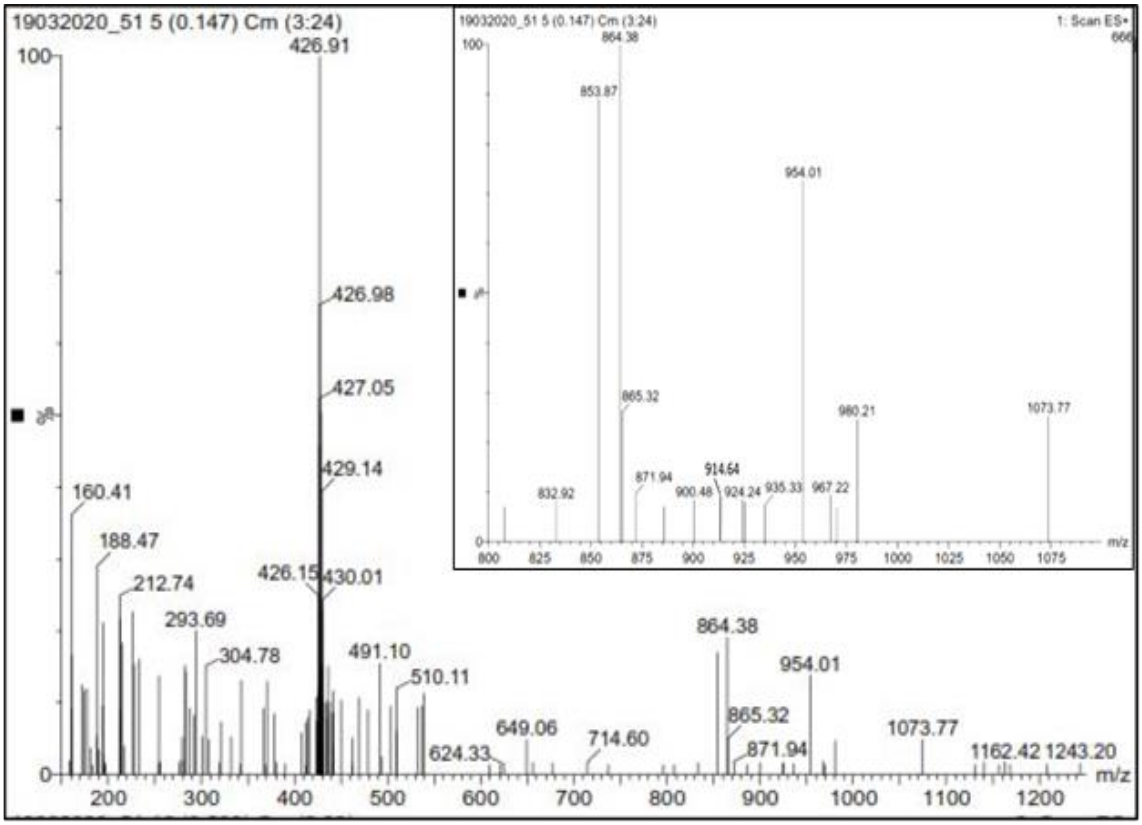

Figure S3.7 ESI-MS spectra of complex 2

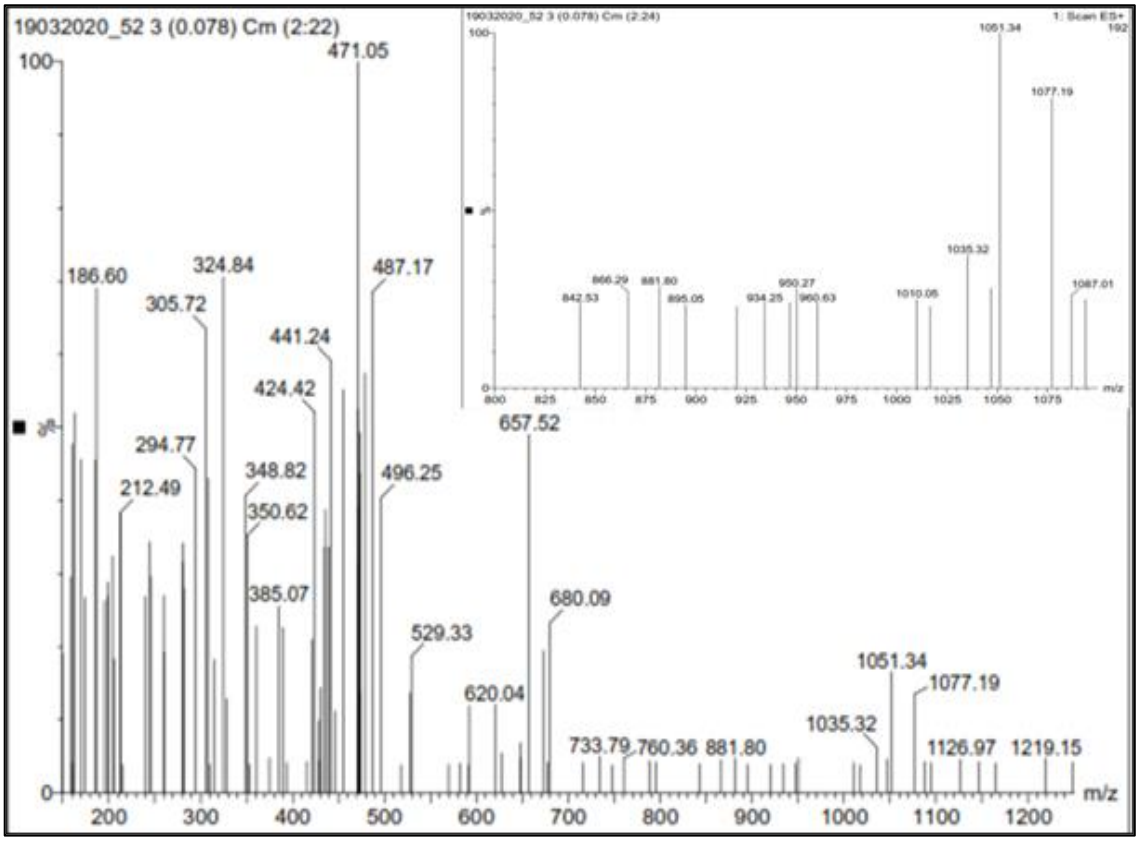

Figure S3.8 ESI-MS spectra of complex 3

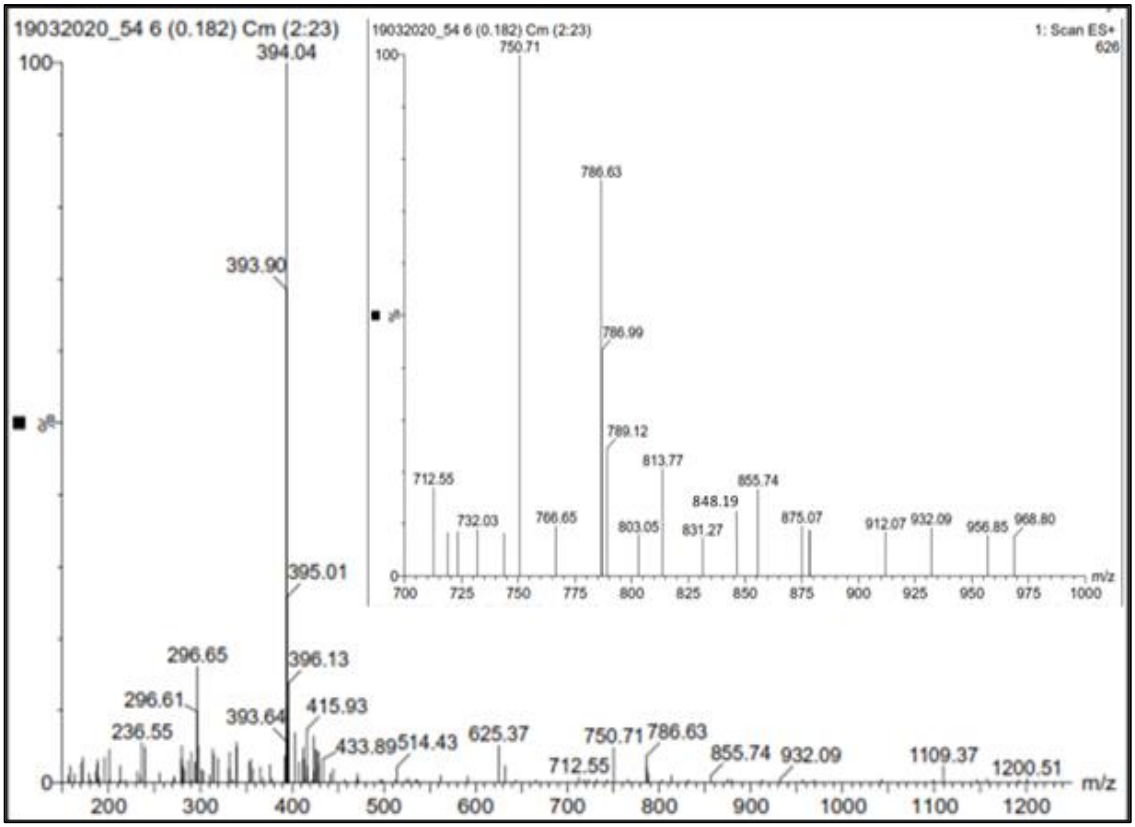

Figure S3.9 ESI-MS spectra of complex 4

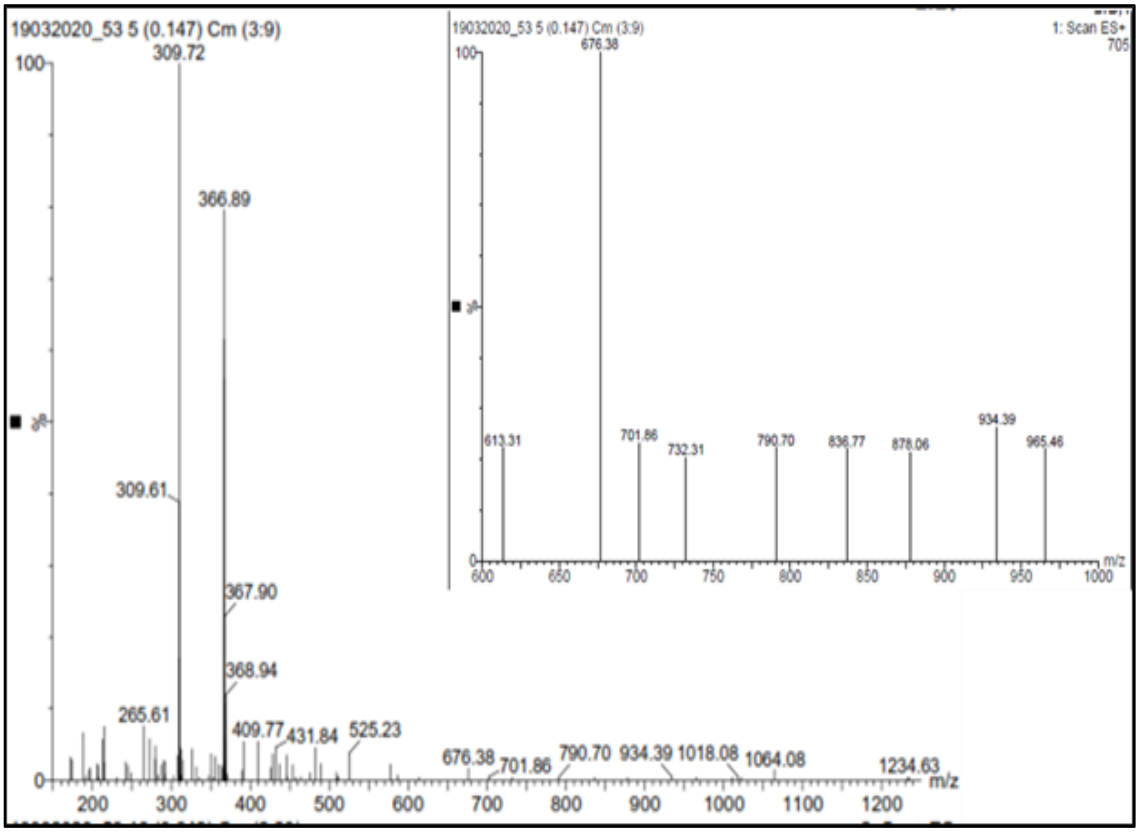

Figure S3.10 ESI-MS spectra of complex 5

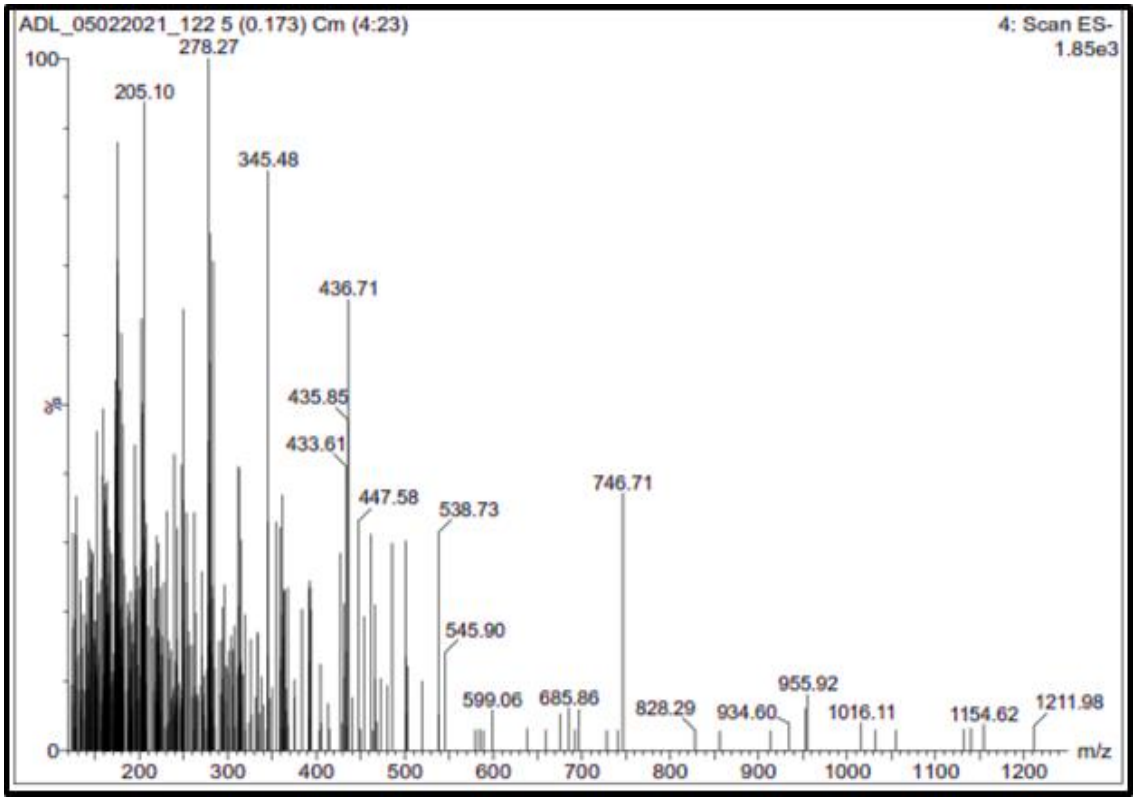

Figure S3.11 ESI-MS spectra of complex 6

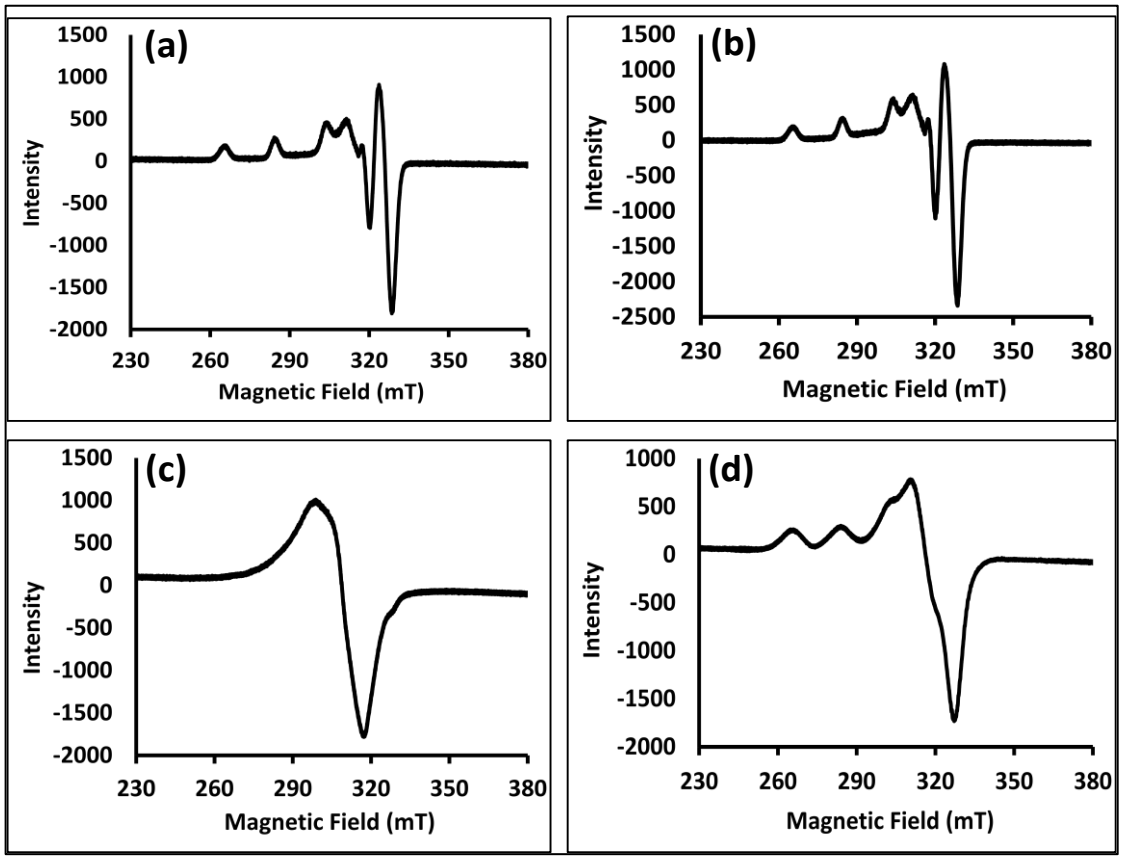

Figure S3.12 EPR spectra of complex (a) 2, (b) 3, (c) 4 and (d) 5

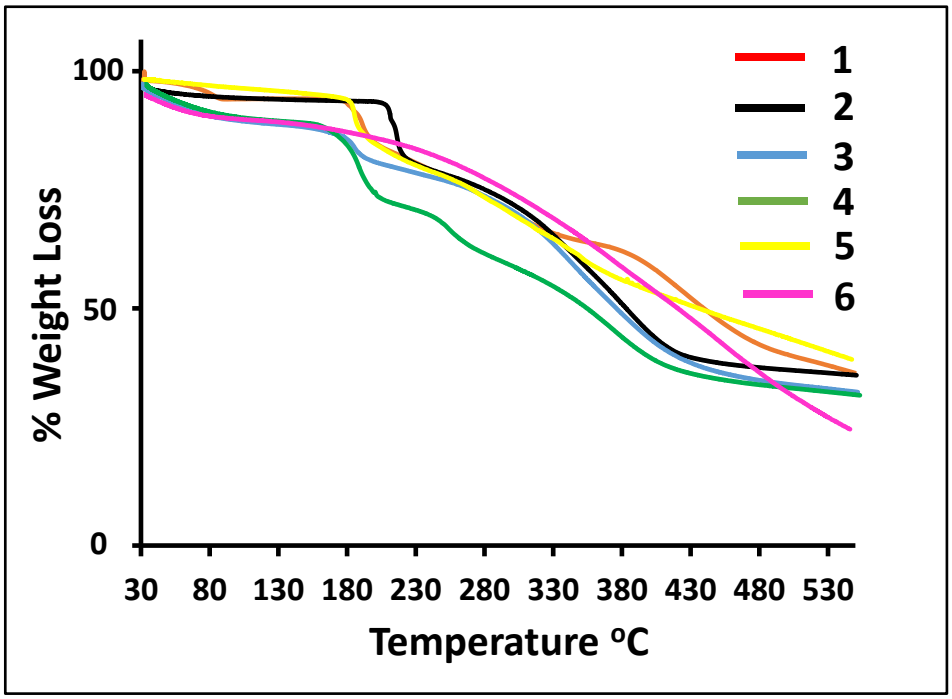

Figure S3.13 TGA plot of complexes 1-6

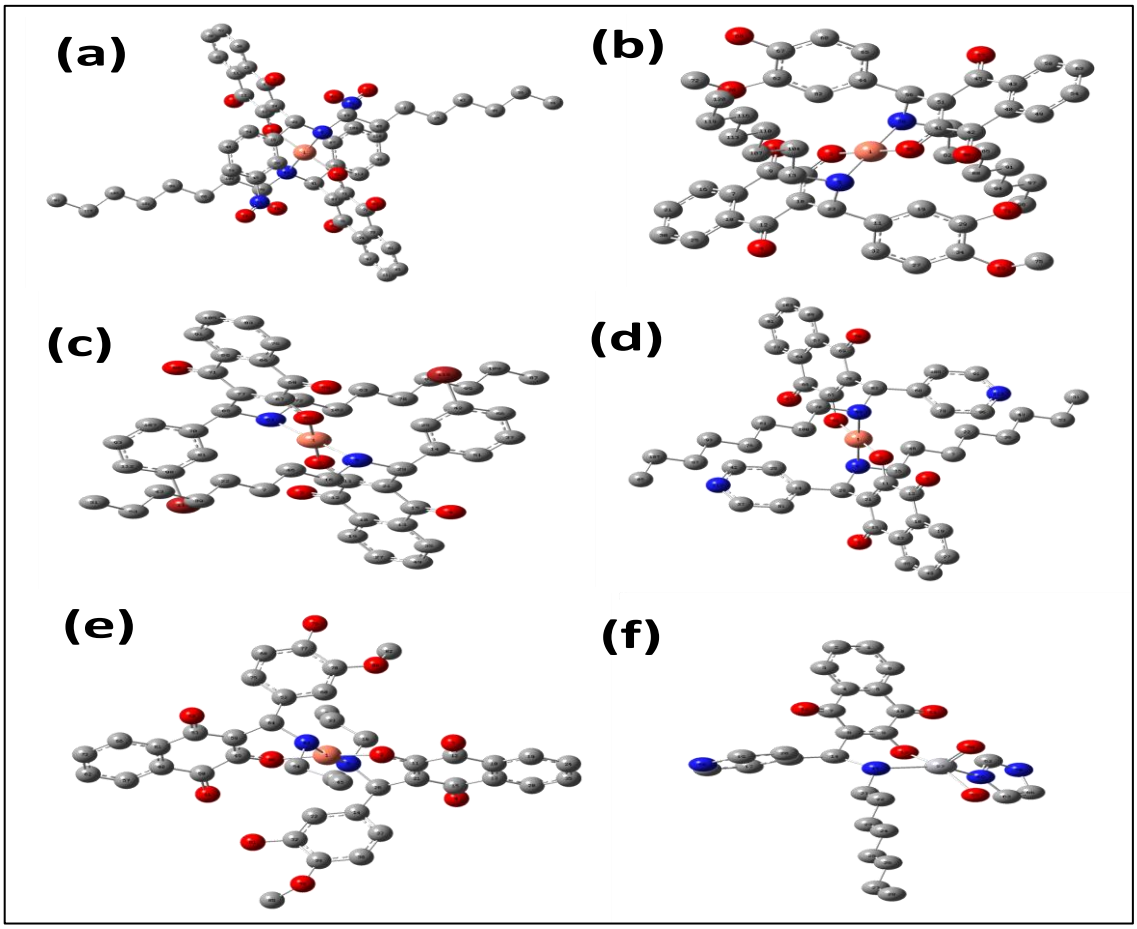

Figure S3.14 Optimized structures of complex (a) 1, (b) 2, (c) 3, (d) 4, (e) 5 and (f) 6

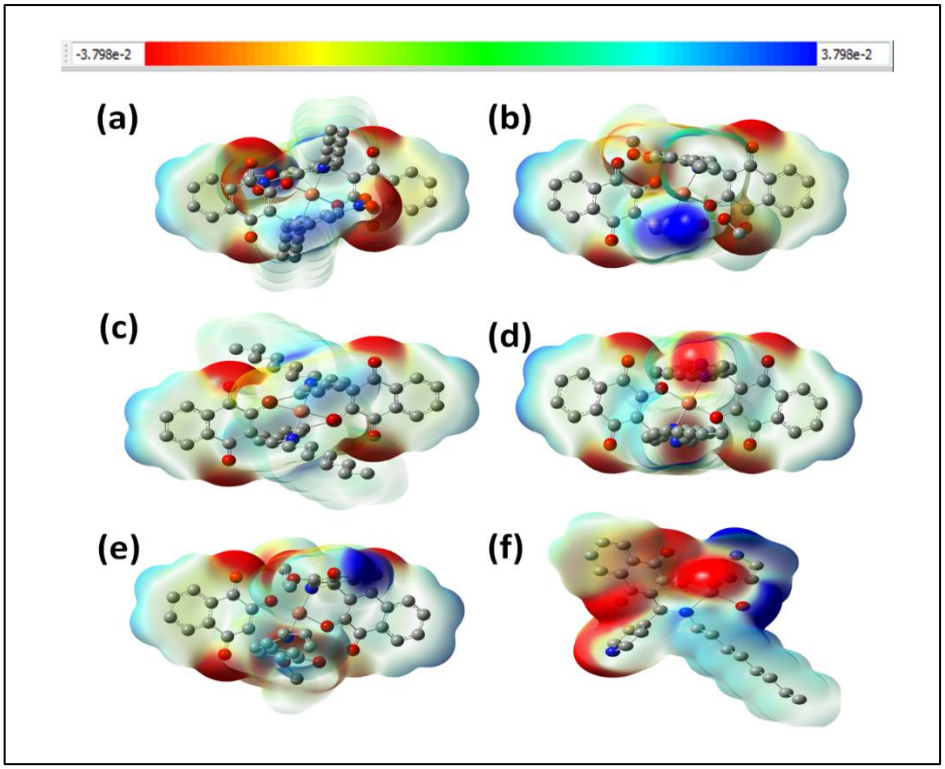

Figure S3.15 MEP diagram of complex (a) 1, (b) 2, (c) 3, (d) 4, (e) 5 and (f) 6

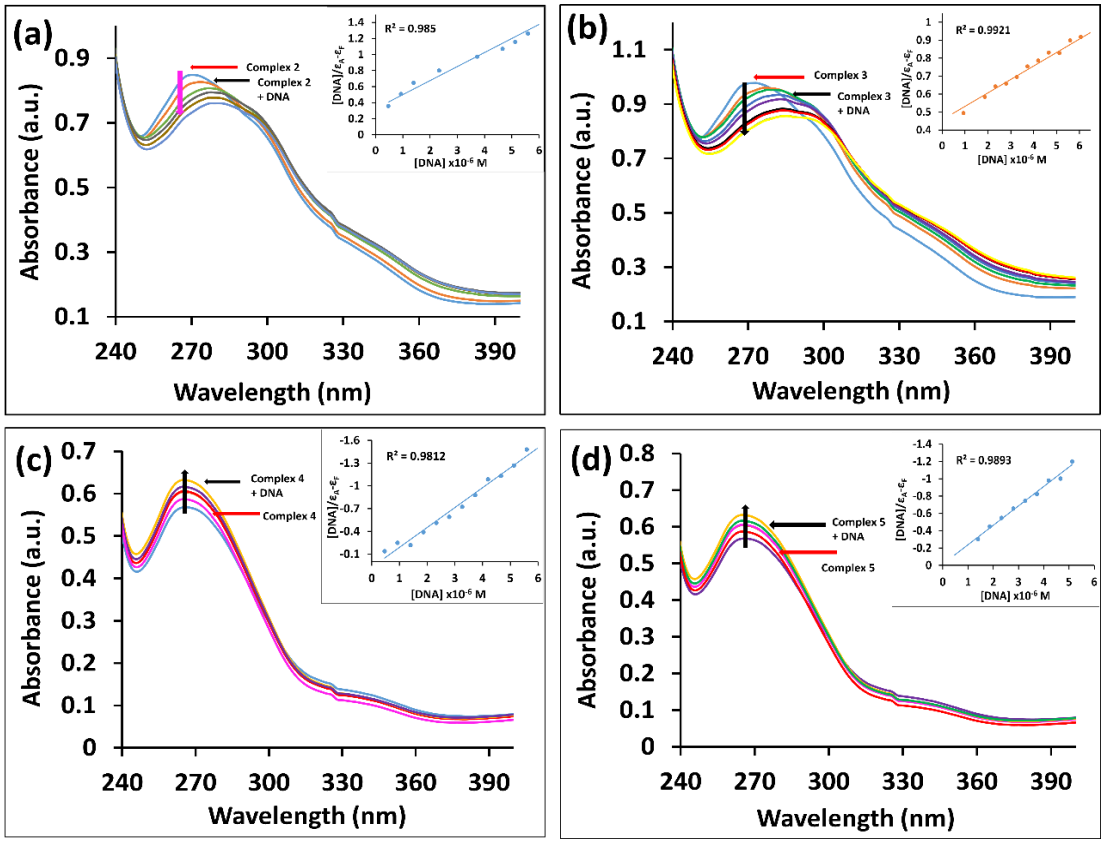

Figure S3.16 UV absorption spectra of complex (a) 2, (b) 3, (c) 4, and (d) 5 at increasing concentration of CT-DNA (inset: Plots of [DNA]/(ε_A-ε_f) vs. [DNA])

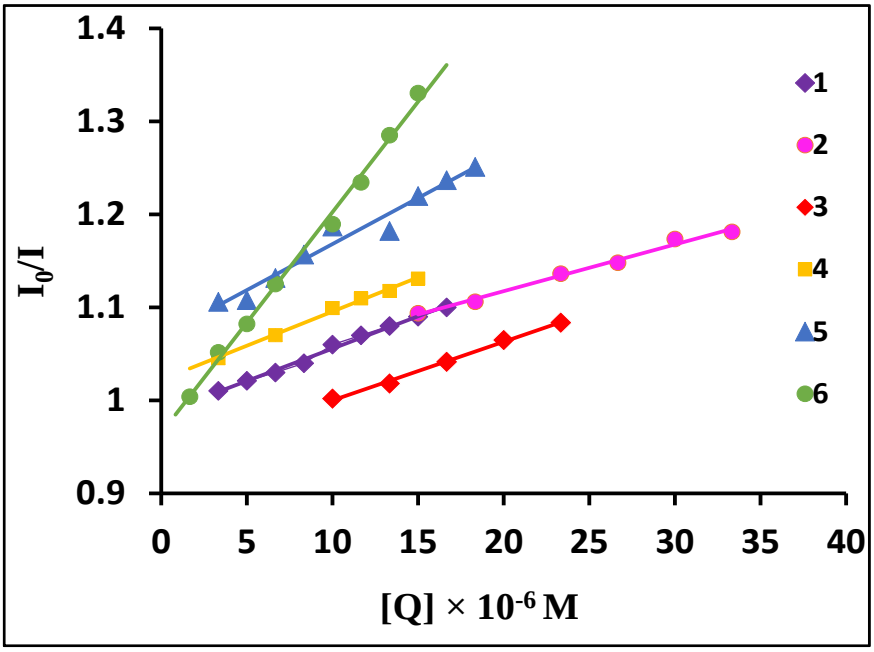

Figure S3.17 Stern-Volmer quenching plot of DNA-EB emission in presence of complex 1-6.

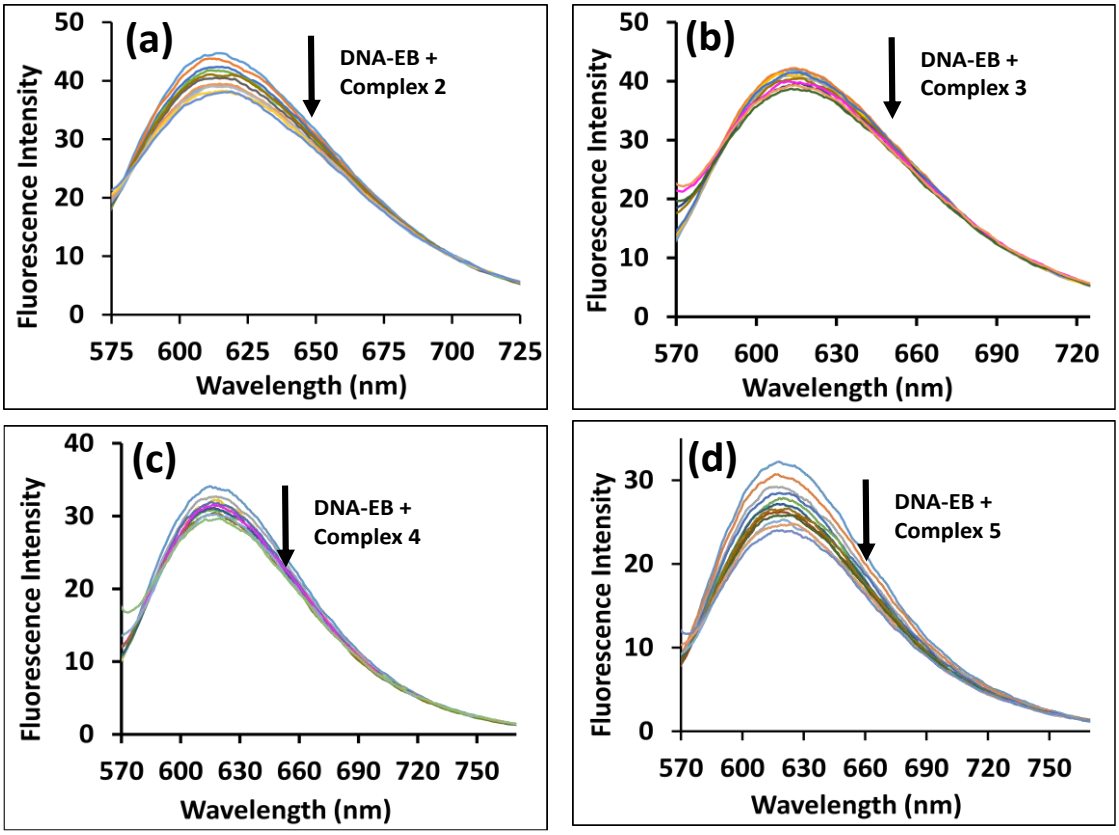

Figure S3.18 Plot of fluorescence emission intensity I *versus* wavelength λ for CT-DNA-EB complex at different concentration of complexes (a) 2, (b) 3, (c) 4, and (d) 5

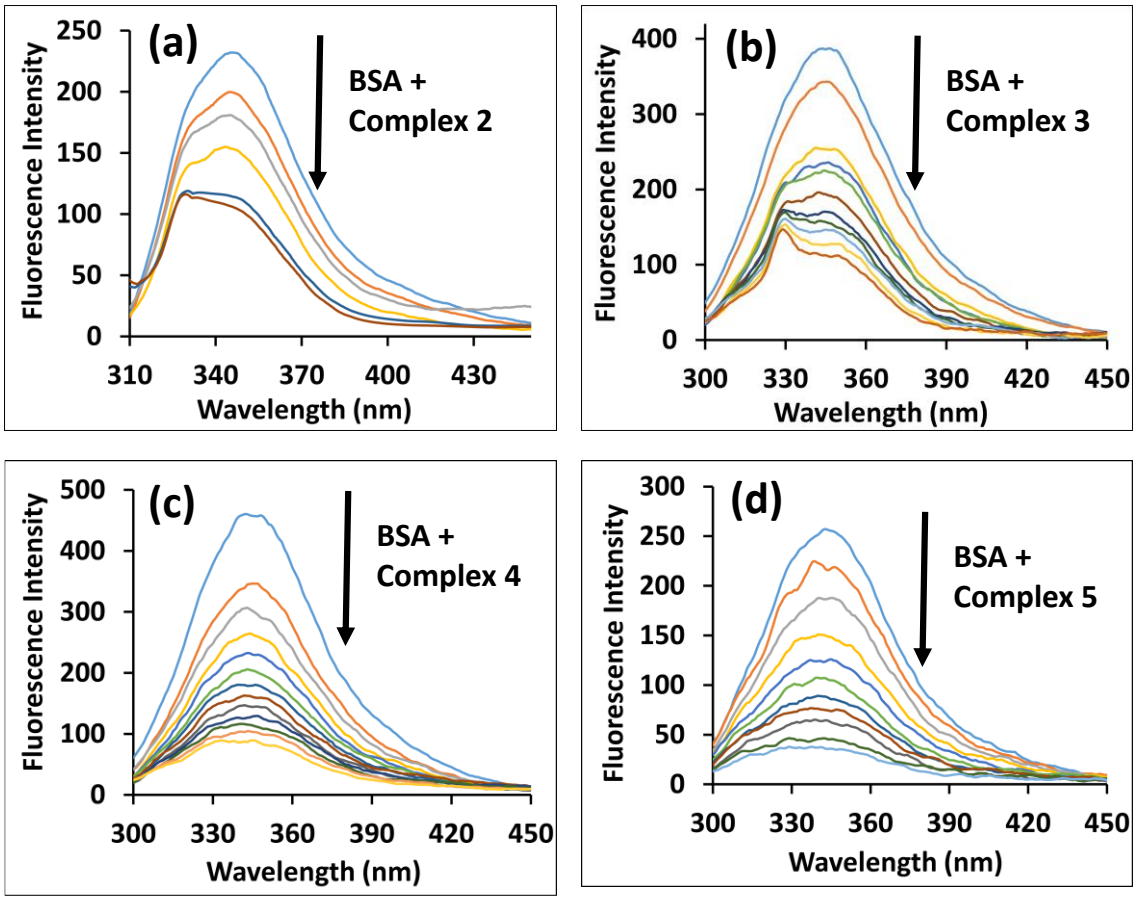

Figure S3.19 Plot of fluorescence emission intensity I *versus* wavelength λ for BSA at increasing concentration of complexes (a) 2, (b) 3, (c) 4 and (d) 5.

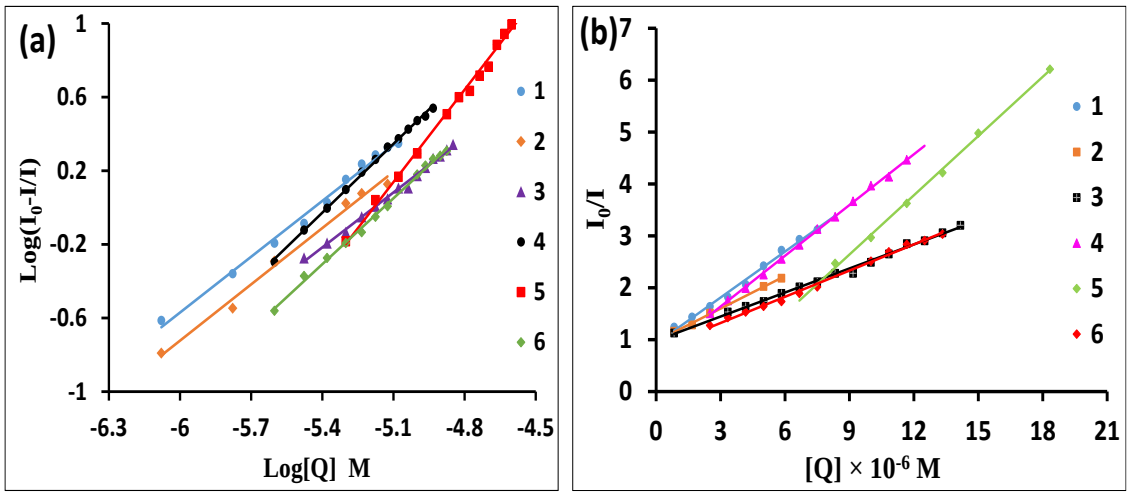

Figure S3.20 Double logarithmic plot for the quenching of BSA fluorescence by complexes 1-6.

Table S3.1 Metal ligand bond length and bond angle of complex 1, 2, 3 and 4 under study obtained from geometry optimization

Complex 2			
Bond length (Å)	R(2,1)	O2-Cu1	1.9289
	R(35,1)	O35-Cu1	2.1493
	R(5,1)	N5-Cu1	1.9454
	R(38,1)	N38-Cu1	2.0467
Bond angle (in °)	A(2,1,35)	O2-Cu1-O35	179.6539
	A(2,1,5)	O2-Cu1-N5	91.3479
	A(2,1,38)	O2-Cu1-N38	88.1869
	A(38,1,35)	O38-Cu1-N35	89.6801
	A(38,1,5)	O35-Cu1-N5	91.537
	A(5,1,35)	N5-Cu1-N35	181.2417
Complex 3			
Bond length (Å)	R(2,1)	O2-Cu1	1.9333
	R(58,1)	O58-Cu1	1.9333
	R(5,1)	N5-Cu1	2.0481
	R(61,1)	N61-Cu1	2.0481
Bond angle (in °)	A(2,1,58)	O2-Cu1-O58	180.021
	A(2,1,5)	O2-Cu1-N5	91.981
	A(2,1,61)	O2-Cu1-N61	88.016
	A(58,1,39)	O58-Cu1-N5	88.068
	A(58,1,61)	O58-Cu1-N61	91.9861
	A(5,1,61)	N5-Cu1-N61	180.003
Complex 4			
Bond length (Å)	R(2,1)	O2-Cu1	1.9606
	R(56,1)	O56-Cu1	1.9606
	R(5,1)	N5-Cu1	2.0895
	R(59,1)	N59-Cu1	2.0894
Bond angle (in °)	A(5,1,59)	N5-Cu1-N59	181.0417
	A(56,1,59)	O56-Cu1-N59	90.981
	A(5,1,56)	N5-Cu1-O56	89.016
	A(2,1,59)	O2-Cu1-N59	88.516
	A(2,1,56)	O2-Cu1-O56	180.523
	A(2,1,5)	O2-Cu1-N5	91.781

3.7 References

1. Tandon, V. K., Yadav, D. B., Chaturvedi, A. K. & Shukla, P. K. Synthesis of (1,4)-naphthoquinono-[3,2-c]-1H-pyrazoles and their (1,4)-naphthohydroquinone derivatives as antifungal, antibacterial, and anticancer agents. *Bioorganic Med. Chem. Lett.* **15**, 3288–3291 (2005).
2. da Silva, G. B., Neves, A. P., Vargas, M. D., Marinho-Filho, J. D. B. & Costa-Lotufo, L. V. New insights into 3-(aminomethyl)naphthoquinones: Evaluation of cytotoxicity, electrochemical behavior and search for structure–activity correlation. *Bioorganic Med. Chem. Lett.* **26**, 3537–3542 (2016).
3. Nariya, P., Shukla, F., Vyas, H., Devkar, R. & Thakore, S. Synthesis and characterization of Mannich bases of lawsone and their anticancer activity. *Synth. Commun.* **50**, 1724–1735 (2020).
4. Neves, A. P. *et al.* Exploring the DNA binding/cleavage, cellular accumulation and topoisomerase inhibition of 2-hydroxy-3-(aminomethyl)-1,4-naphthoquinone Mannich bases and their platinum(II) complexes. *J. Inorg. Biochem.* **119**, 54–64 (2013).
5. Oliveira, K. M. *et al.* Selective Ru(II)/lawsone complexes inhibiting tumor cell growth by apoptosis. *J. Inorg. Biochem.* **176**, 66–76 (2017).
6. Kubanik, M. *et al.* Towards targeting anticancer drugs: Ruthenium(II)-arene complexes with biologically active naphthoquinone-derived ligand systems. *Dalt. Trans.* **45**, 13091–13103 (2016).
7. Ahmad, A. *et al.* New ferrocene modified lawsone Mannich bases with anti-proliferative activity against tumor cells. *J. Saudi Chem. Soc.* **21**, 105–110 (2017).
8. Xu, L. *et al.* Temperature-Responsive Multilayer Films of Micelle-Based Composites for Controlled Release of a Third-Generation EGFR Inhibitor. *ACS Appl. Polym. Mater.* **2**, 741–750 (2020).
9. Guo, Y., Hu, X., Zhang, X., Pu, X. & Wang, Y. The synthesis of a Cu(ii) Schiff base complex using a bidentate N2O2 donor ligand: Crystal structure, photophysical properties, and antibacterial activities. *RSC Adv.* **9**, 41737–41744 (2019).
10. Dankhoff, K. *et al.* Copper(ii) complexes with tridentate Schiff base-like ligands: Solid state and solution structures and anticancer activity. *Dalt. Trans.* **48**, 15220–15230 (2019).

11. Goldwaser, I., Gefel, D., Gershonov, E., Fridkin, M. & Shechter, Y. Insulin-like effects of vanadium: basic and clinical implications. *J. Inorg. Biochem.* **80**, 21–25 (2000).
12. Banerjee, A. *et al.* Synthesis, structure and characterization of new dithiocarbazate-based mixed ligand oxidovanadium(iv) complexes: DNA/HSA interaction, cytotoxic activity and DFT studies. *New J. Chem.* **44**, 10946–10963 (2020).
13. Rehder, D. The medicinal and catalytic potential of model complexes of vanadate-dependent haloperoxidases. *Coord. Chem. Rev.* **237**, 53–63 (2003).
14. Neves, A. P. *et al.* Novel aminonaphthoquinone Mannich bases derived from lawsone and their copper(II) complexes: Synthesis, characterization and antibacterial activity. *J. Braz. Chem. Soc.* **20**, 712–727 (2009).
15. Han, H. *et al.* Synthesis and evaluation of oxovanadium(iv) complexes of Schiff-base condensates from 5-substituted-2-hydroxybenzaldehyde and 2-substituted-benzenamine as selective inhibitors of protein tyrosine phosphatase 1B. *Dalt. Trans.* **41**, 11116 (2012).
16. Zabierowski, P., Szklarzewicz, J., Kurpiewska, K., Lewiński, K. & Nitek, W. Assemblies of substituted salicylidene-2-ethanolamine copper(II) complexes: From square planar monomeric to octahedral polymeric halogen analogues. *Polyhedron* **49**, 74–83 (2013).
17. Muppidi, V. K., Das, S., Raghavaiah, P. & Pal, S. Copper(II) complexes with chiral reduced Schiff bases: Helical self-assembly via intermolecular C-H···O interactions. *Inorg. Chem. Commun.* **10**, 234–238 (2007).
18. Muppidi, V. K., Zacharias, P. S. & Pal, S. Metal-organic frameworks from chiral square-pyramidal copper(II) complexes: Enantiospecific inclusion and perfectly polar alignment of guest and host molecules. *J. Solid State Chem.* **180**, 132–137 (2007).
19. Thakuria, H. & Das, G. CuO micro plates from a 3D metallo-organic framework (MOF) of a binary copper(II) complex of N,N-bis(2-hydroxyethyl)glycine. *Polyhedron* **26**, 149–153 (2007).
20. Yang, P. *et al.* Copper(ii) complexes with NNO ligands: Synthesis, crystal structures, DNA cleavage, and anticancer activities. *Dalt. Trans.* **48**, 17925–17935 (2019).

21. Arjmand, F., Afsan, Z. & Roisnel, T. Design, synthesis and characterization of novel chromone based-copper(ii) antitumor agents with N,N-donor ligands: comparative DNA/RNA binding profile and cytotoxicity. *RSC Adv.* **8**, 37375–37390 (2018).
22. Loganathan, R. *et al.* DNA and protein binding, double-strand DNA cleavage and cytotoxicity of mixed ligand copper(II) complexes of the antibacterial drug nalidixic acid. *J. Inorg. Biochem.* **174**, 1–13 (2017).
23. Yuan, C. *et al.* Synthesis, characterization, and protein tyrosine phosphatases inhibition activities of oxovanadium(IV) complexes with Schiff base and polypyridyl derivatives. *J. Inorg. Biochem.* **104**, 978–986 (2010).
24. Lu, L. *et al.* Inhibition protein tyrosine phosphatases by an oxovanadium glutamate complex, Na2[VO(Glu)2(CH3OH)](Glu = glutamate). *BioMetals* **23**, 1139–1147 (2010).
25. Khadtare, S. S. *et al.* Dye sensitized solar cell with lawsone dye using a ZnO photoanode: Experimental and TD-DFT study. *RSC Adv.* **5**, 17647–17652 (2015).
26. Neves, A. P. *et al.* Dinuclear copper(II) complexes of a novel 3-(aminomethyl)naphthoquinone Mannich base: Synthesis, structural, magnetic and electrochemical studies. *Polyhedron* **29**, 2884–2891 (2010).
27. Garribba, E., Micera, G., Panzanelli, A. & Sanna, D. Electronic Structure of Oxovanadium(IV) Complexes of α-Hydroxycarboxylic Acids. *Inorg. Chem.* **42**, 3981–3987 (2003).
28. Hussain, A. *et al.* Copper(II) complexes as potential anticancer and Nonsteroidal anti-inflammatory agents: In vitro and in vivo studies. *Sci. Rep.* **9**, 1–17 (2019).
29. Paquet, C. *et al.* The role of amine ligands in governing film morphology and electrical properties of copper films derived from copper formate-based molecular inks. *Nanoscale* **10**, 6911–6921 (2018).
30. J, D. Synthesis, Crystal Structure, and Electronic Properties of (L-Methionylglycinato)copper(II). *Inorg. Chem.* **18**, 1543 (1979).
31. Syiemlieh, I., Asthana, M., Kurbah, S. D. & Lal, R. A. Synthesis, crystal structure and reactivity of homobimetallic vanadium(V) complexes derived from oxaloyldihydrazone ligands. *Polyhedron* **170**, 202–216 (2019).
32. Frenzel, N., Hartley, J. & Frisch, G. Voltammetric and spectroscopic study of ferrocene and hexacyanoferrate and the suitability of their redox couples as

internal standards in ionic liquids. *Phys. Chem. Chem. Phys.* **19**, 28841–28852 (2017).

33. Borthakur, R., Kumar, A., De, A. K. & Lal, R. A. Synthesis, characterization and electrochemical properties of copper(II) complexes derived from succinoyldihydrazine Schiff base ligands. *Arab. J. Chem.* **12**, 2192–2205 (2019).
34. Manimaran, A., Prabhakaran, R., Deepa, T., Natarajan, K. & Jayabalakrishnan, C. Synthesis, spectral characterization, electrochemistry and catalytic activities of Cu(II) complexes of bifunctional tridentate Schiff bases containing O - NO donors. *Appl. Organomet. Chem.* **22**, 353–358 (2008).
35. Elamathi, C., Fronczek, F. R., Madankumar, A. & Prabhakaran, R. Synthesis and spectral characterizations of water soluble Cu(ii) complexes containing N-heterocyclic chelates: cell-proliferation, antioxidant and nucleic acid/serum albumin interactions. *New J. Chem.* **44**, 4158–4170 (2020).
36. Nasibipour, M., Safaei, E., Wrzeszcz, G. & Wojtczak, A. Tuning of the redox potential and catalytic activity of a new Cu(ii) complex by: O - iminobenzosemiquinone as an electron-reservoir ligand. *New J. Chem.* **44**, 4426–4439 (2020).
37. Vijayan, P. *et al.* Nickel(ii) and copper(ii) complexes constructed with N2S2 hybrid benzamidine-thiosemicarbazone ligand: Synthesis, X-ray crystal structure, DFT, kinetico-catalytic and in vitro biological applications. *RSC Adv.* **5**, 103321–103342 (2015).
38. Chang, Y. P., Furness, L., Levason, W., Reid, G. & Zhang, W. Complexes of vanadium(IV) oxide difluoride with neutral N- and O-donor ligands. *J. Fluor. Chem.* **191**, 149–160 (2016).
39. Yaul, A., Pethe, G., Deshmukh, R. & Aswar, A. Vanadium complexes with quadridentate Schiff bases: Synthesis, characterization, thermal and catalytic studies. *J. Therm. Anal. Calorim.* **113**, 745–752 (2013).
40. Murugavel, S., Ravikumar, C., Jaabil, G. & Alagusundaram, P. Synthesis, crystal structure analysis, spectral investigations (NMR, FT-IR, UV), DFT calculations, ADMET studies, molecular docking and anticancer activity of 2-(1-benzyl-5-methyl-1H-1,2,3-triazol-4-yl)-4-(2-chlorophenyl)-6-methoxypyridine – A novel poten. *J. Mol. Struct.* **1176**, 729–742 (2019).
41. Krishnan, K. G. *et al.* Novel cyanoacetamide integrated phenothiazines: Synthesis,

characterization, computational studies and in vitro antioxidant and anticancer evaluations. *J. Mol. Struct.* **1199**, 127037 (2020).

42. Khan, I. M. & Shakya, S. Exploring Colorimetric Real-Time Sensing Behavior of a Newly Designed CT Complex toward Nitrobenzene and Co2+: Spectrophotometric, DFT/TD-DFT, and Mechanistic Insights. *ACS Omega* **4**, 9983–9995 (2019).
43. Jawaria, R. *et al.* Synthesis, crystal structure analysis, spectral characterization and nonlinear optical exploration of potent thiosemicarbazones based compounds: A DFT refine experimental study. *Inorganica Chim. Acta* **486**, 162–171 (2019).
44. Khan, I. M. *et al.* Exploring interaction dynamics of designed organic cocrystal charge transfer complex of 2-hydroxypyridine and oxalic acid with human serum albumin: Single crystal, spectrophotometric, theoretical and antimicrobial studies. *Bioorg. Chem.* **100**, 103872 (2020).
45. Rocha, M. *et al.* Diethylaminophenyl-based Schiff base Cu(ii) and V(iv) complexes: Experimental and theoretical studies and cytotoxicity assays. *New J. Chem.* **43**, 18832–18842 (2019).
46. Kumar, M., Kumar, G. & Masram, D. T. Copper(ii) complexes containing enoxacin and heterocyclic ligands: Synthesis, crystal structures and their biological perspectives. *New J. Chem.* **44**, 8595–8613 (2020).
47. Zampakou, M. *et al.* Structure, antimicrobial activity, albumin- and DNA-binding of manganese(<scp>ii</scp>)–sparfloxacinato complexes. *RSC Adv.* **5**, 11861–11872 (2015).
48. Draksharapu, A. *et al.* Binding of Copper(II) Polypyridyl Complexes to DNA and Consequences for DNA-based Asymmetric Catalysis. *Dalt. Trans.* **44**, 3647–3655 (2015).
49. Novotný, J., Bazzi, S., Marek, R. & Kozelka, J. Lone-pair–π interactions: analysis of the physical origin and biological implications. *Phys. Chem. Chem. Phys.* **18**, 19472–19481 (2016).
50. Mudavath, R. *et al.* Molecular docking, QSAR properties and DNA/BSA binding, anti-proliferative studies of 6-methoxy benzothiozole imine base and its metal complexes. *J. Biomol. Struct. Dyn.* **38**, 2849–2864 (2020).
51. Kumar, M., Kumar, G., Dadure, K. M. & Masram, D. T. Copper(II) complexes based on levofloxacin and 2N-donor ligands: synthesis, crystal structures and in

vitro biological evaluation. *New J. Chem.* **43**, 15462–15481 (2019).

52. Niu, M. *et al.* DNA/protein interaction, cytotoxic activity and magnetic properties of amino-alcohol Schiff base derived Cu(ii)/Ni(ii) metal complexes: influence of the nuclearity and metal ions. *RSC Adv.* **5**, 37085–37095 (2015).
53. Santini, C. *et al.* Advances in copper complexes as anticancer agents. *Chem. Rev.* **114**, 815–862 (2014).
54. Sathyadevi, P. *et al.* Effect of substitution and planarity of the ligand on DNA/BSA interaction, free radical scavenging and cytotoxicity of diamagnetic Ni(ii) complexes: A systematic investigation. *Dalt. Trans.* **40**, 9690 (2011).
55. Krishnamoorthy, P. *et al.* Copper(i) and nickel(ii) complexes with 1 : 1 vs. 1 : 2 coordination of ferrocenyl hydrazone ligands: Do the geometry and composition of complexes affect DNA binding/cleavage, protein binding, antioxidant and cytotoxic activities? *Dalt. Trans.* **41**, 4423 (2012).
56. Joksimović, N. *et al.* Synthesis, characterization, biological activity, DNA and BSA binding study: Novel copper(II) complexes with 2-hydroxy-4-aryl-4-oxo-2-butenoate. *Dalt. Trans.* **45**, 15067–15077 (2016).
57. Gomathi Sankareswari, V. *et al.* Interaction of oxovanadium(iv)–salphen complexes with bovine serum albumin and their cytotoxicity against cancer. *Dalt. Trans.* **43**, 3260–3272 (2014).
58. Pascale, F., Bedouet, L., Baylatry, M., Namur, J. & Laurent, A. Comparative chemosensitivity of VX2 and HCC cell lines to drugs used in TACE. *Anticancer Res.* **35**, 6497–6504 (2015).
59. Dolomanov, O. V., Bourhis, L. J., Gildea, R. J., Howard, J. A. K. & Puschmann, H. OLEX2: A complete structure solution, refinement and analysis program. *J. Appl. Crystallogr.* **42**, 339–341 (2009).
60. Sheldrick, G. M. Crystal structure refinement with SHELXL. *Acta Crystallogr. Sect. C Struct. Chem.* **71**, 3–8 (2015).
61. Khan, I. M. *et al.* Synthesis, characterization, antimicrobial and DNA binding properties of an organic charge transfer complex obtained from pyrazole and chloranilic acid. *Bioorg. Chem.* **99**, 103779 (2020).
62. Martins, N. M. R. *et al.* DNA and BSA binding and cytotoxic properties of copper(II) and iron(III) complexes with arylhydrazone of ethyl 2-cyanoacetate or formazan ligands. *New J. Chem.* **41**, 4076–4086 (2017).